Effect of the Injection Scenario on the Rate and Magnitude Content of Injection-Induced Seismicity: Case of a Heterogeneous Fault

Almakari Michelle[1] [ID] **, Dublanchet Pierre[1], Chauris Hervé[1]** [ID] **, and Pellet Frédéric[1]** [ID]

[1]MINES ParisTech, PSL University, Centre de géosciences, Fontainebleau, France

Abstract Injection of fluids into underground formations reactivates preexisting faults and modifies the seismic hazard, as demonstrated by the 2011 M_w 5.7 and the 2016 M_w 5.8 earthquakes in Oklahoma. Currently, the effect of injection remains poorly understood. We model the seismicity triggered by a fluid flowing inside a Dietrich-Ruina heterogeneous 2-D fault, which can generate irregular sequences of events with magnitudes obeying Gutenberg Richter distribution. We consider a punctual injection scenario where injection pressure increases at a constant rate until a maximum pressure is reached and kept constant. We show that such a fluid injection leads to a sharp increase in the seismicity rate, which correlates with the time series of the pore pressure rate, for a wide range of injection pressure. Increasing the final pressure leads to an increase in the amplitude and the duration of the seismicity rate perturbation but also to a decrease in the frequency of large-magnitude events. The maximum seismicity rate during the sequence also increases with the injection pressure rate, as long as a pressure-rate threshold is not exceeded. Beyond it, the effect of increasing the injection rate is to make large-magnitude earthquakes more frequent. While the total number of induced earthquakes is essentially controlled by the maximum pressure, the total seismic moment liberated increases with both the maximum pressure and the pressure rate. The comparison of our model to Dietrich's (1994, https://doi.org/10.1029/93JB02581) model shows the important trade-off existing between seismicity rate perturbations and magnitude content variations of fluid induced seismicity.

1. Introduction

It has been acknowledged, since the 1960s, that injection of fluids into underground formations alters the stresses on the Earth's crust, inducing micro-earthquakes and modifying the seismic hazard (Simpson, 1986). Fluid injection could be related to different human activities, such as wastewater disposal (Ellsworth, 2013; Healy et al., 1968; Horton, 2012), hydrofracturing (Holland, 2011; Kanamori & Hauksson, 1992) and production of geothermal energy (Bachmann et al., 2011; Deichman & Giardini, 2009; Majer et al., 2007). Wastewater disposal seems to represent the highest risk, as it operates for longer duration and injects much more fluid (Ellsworth, 2013).

Beyond microseismic activities, many significant earthquakes were suspected to be injection-induced events, with moment magnitudes exceeding 3: the M_w 4.85 in Rocky mountain arsenal (Healy et al., 1968; Hermann et al., 1981), the 1967 M_w 5.5 in Denver Colorado (Davis & Frohlich, 1993; Healy et al., 1968), the four M_w 3 in Basel, Switzerland, between 2006 and 2007 (Deichman & Giardini, 2009), the 2011 M_w 4.7 in Guy, Arkansas (Horton, 2012), the 2011 M_w 5.3 in Trinidad, Colorado (Rubinstein et al., 2012; Viegas et al., 2012), the 2011 M_w 3.9 in Youngstown, Ohio (Kim, 2013; Skoumal et al., 2014), the M_w 5.7 in Prague, Oklahoma in 2011 (Keranen et al., 2013; McGarr, 2014; Sumy et al., 2014; Van der Elst et al., 2013), the 2011 and 2012 M_w 4.8 in Texas (Frohlich et al., 2014), and the 2016 M_w 5.8 earthquake in Pawnee, Oklahoma (Yeck et al., 2016).

According to Healy et al. (1968) and Raleigh et al. (1976), injection-induced earthquakes correspond to fault reactivation, triggered by an increase of the fluid pore pressure. In fact, the failure along the fault is reached when the stress on the fault exceeds its frictional strength τ. The latter is proportional to the effective normal stress (Byerlee, 1978), following

$$\tau = \tau_0 + \sigma_{\text{eff}}\mu, \tag{1}$$

where τ_0 is the cohesive strength, σ_{eff} the effective normal stress ($\sigma_{\text{eff}} = \sigma_T - p$), μ is the friction coefficient, σ_T the lithostatic normal stress, and p the pore pressure. Thus, an increase of pore pressure can decrease the effective normal stress and consequently decrease the frictional strength on a fault close to failure. Some authors argue that earthquakes are triggered if the pore pressure exceeds a critical pressure threshold (Healy et al., 1968; Hubert & Rubey, 1959; Raleigh et al., 1976), while Frohlich (2012) considers that a seismic event can be induced when the injection rate reaches a critical rate and the permeability of the medium allows the fluids to reach a suitably oriented fault.

Even though it has been acknowledged that injection-induced earthquakes are caused by either direct pore pressure effects or poroelastic stress changes, currently, the main controlling parameters of injection-induced seismicity remain poorly understood. With the increasing number of induced earthquakes, it is crucial to identify the key parameters governing this phenomenon. The injection scenario, in terms of injection pressure or injection rate, was observed to be an essential parameter controlling the induced seismicity. For instance, Frohlich (2012) observed that fluid injection can induce seismicity only if the injection pressure and injection rate are large enough, in the presence of a favorably oriented fault. It was also observed that the seismicity in Oklahoma rose 20 years after injection started but only 5 years after an abrupt increase in the wellhead pressure (Keranen et al., 2013). On the other hand, Langenbruch and Zoback (2016) proposed a diffusion model for the seismicity in Oklahoma that can explain the previous induced seismic sequences and found that by decreasing the injection rate, the pore pressure rate at 3-km depth can decrease and can lead to a drop in the seismicity rate. Dempsey and Riffault (2019) proposed a numerical model for the seismicity rate in Oklahoma and also showed that a reduction in injection rate may lead to a decrease in the seismicity rate, while the characteristic time to reach the background seismicity level depends on the magnitude of the injection rate reduction.

Many numerical models have been proposed to study the reactivation of fault slip and the triggering of seismic activity, such as spring slider systems (Baisch et al., 2010) or a homogeneous planar fault (Aochi et al., 2014), both governed by Coulomb friction. In the latter case, the friction μ is considered to be constant, and thus time-dependent characteristics of fault friction (healing for instance) are not taken into account. Alternatively, rate- and state-dependent friction law (Dietrich, 1979; Ruina, 1983) considers the effects of both sliding speed and the history of the sliding surface and allows for healing and multiple successive reactivations. It is therefore better suited to explain features of the earthquake cycle. Various models based on the rate- and state-dependent friction have been developed, like a multidegree of freedom spring-slider system by Turuntaev and Riga (2017), a homogeneous rate-weakening fault by Kroll et al. (2017) and McClure and Horne (2011), or based on the seismicity rate model proposed by Dietrich (1994) as Segall and Lu (2015), Barbour et al. (2017) and Chang et al. (2018). But these models either have not fully explored the role of injection history or considered simplified stress interactions. The alternative modelling approach by Garagash and Germanovish (2012) and Azad et al. (2017) is to study the effect of hydrofracturing on the onset of dynamic slip, but in their model the seismic cycle was not modeled: It is not possible to determine the magnitudes or the rate of the induced seismicity. Some of these latter models studied the effect of changing the flow rate on the induced seismicity. In particular, Barbour et al. (2017) showed that for an equivalent injected volume, a variable injection rate may lead to a larger seismicity rate increase compared to the one under constant injection rate, while Chang et al. (2018) showed that a gradual decrease in injection rate can reduce postinjection seismicity rate. However, none of these two models take into consideration the magnitude content of the induced seismic events. On the other hand, Rutqvist et al. (2013) investigated the effect of variable injection rate on the magnitude of the seismic rupture in the context of hydraulic fracturing of shale gas reservoirs; however, this study only focused on the first hydraulic rupture. More extensive work is needed to fully understand the role of the different injection parameters on the different features of seismic activity.

Here we systematically study the effect of the fluid injection scenario on the features of induced seismic activity along a planar heterogeneous fault with rate- and state-dependent friction (Dietrich, 1979; Ruina, 1983), and effective normal stress dependent state variable (Linker & Dietrich, 1992). Our model considers fault frictional heterogeneous behavior, so as to produce a realistic seismic activity in terms of seismicity rate and magnitude distribution. We couple a 2-D rate- and state-dependent asperity model (Dublanchet, 2018), with a 1-D fluid diffusion model along the fault segment. We test over 196 different injection scenarios by changing the injection rate, the maximum pressure at the well head, and the diffusive boundary conditions. We aim to define the principal parameters controlling the rate and the magnitudes of induced events.
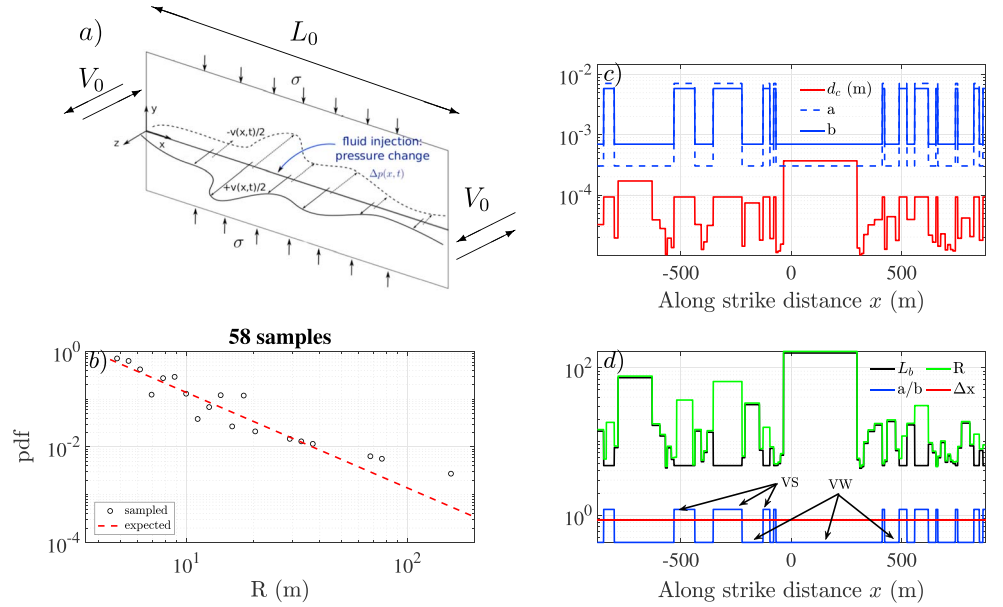
Figure 1. Fault model: (a) Fault system (Mode III): Geometry, slip rate V, length of the fault L_0 ($\approx$ 1.75 km, from Table 1), and boundary conditions (far-field normal stress σ and constant slipping rate V_0 at the edges of the model, values in Table 1), modified from Dublanchet (2018). (b) Frequency distribution of the half lengths R of the fault patches. (c) Distribution of a and b rate- and state-dependent frictional parameters, as well as the critical slip distance d_c along the fault. (d) Distribution of the patch half size R, $L_b = Gd_c/b\sigma$, the ratio of frictional parameters a/b, and the computational cell size Δx, along the fault.

2. Model

We consider a linear planar heterogeneous fault sheared between two 2-D elastic half-spaces (Figure 1a). The fault slips in mode III. Outside a finite segment of size L_0 (in this study $L_0 = 1,754.5$ m; see Table 1), we assume a constant slip rate V_0 ($V_0 = 10^{-9}$ m/s), while inside the finite segment, slip is resisted by heterogeneous rate- and state- dependent friction, defined as

$$\tau = \sigma_{\text{eff}}\mu = \sigma_{\text{eff}}\left[\mu_0 + a(x)\ln\left(\frac{V}{V_0}\right) + b(x)\ln\left(\frac{V_0\theta}{d_c(x)}\right)\right], \tag{2}$$

where $\tau = \tau(x, t)$ is the frictional strength depending on time t and along strike distance x, $\sigma_{\text{eff}} = \sigma_{\text{eff}}(x, t)$ is the effective normal stress ($\sigma_{\text{eff}}(x, t) = \sigma_T - p(x, t)$, where σ_T is a constant lithostatic normal stress and $p(x, t)$ in the pore pressure), $\mu = \mu(x, t)$ is the friction, μ_0 is the reference friction coefficient, $a(x)$ and $b(x)$ are the constitutive parameteres, $V = V(x, t)$ is the sliding velocity, $\theta = \theta(x, t)$ is the state variable, and $d_c(x)$ is the characteristic distance. Dietrich (1979) and Ruina (1983) interpreted the state variable as a characteristic contact lifetime and proposed an evolution law, called aging law:

$$\frac{\mathrm{d}\theta}{\mathrm{d}t} = 1 - \frac{V\theta}{d_c}, \tag{3}$$

where state and thus friction evolve even with stationary contact. According to Rice and Ruina (1983), the state evolution law may also depend on prior normal stress. Following a step increase or decrease in normal stress, the state variable (and consequently shear strength) experiences a sudden increase, or decrease, respectively (Linker & Dietrich, 1992). This effect could be formulated as

$$\frac{\mathrm{d}\theta}{\mathrm{d}\sigma} = -\frac{\alpha\theta}{b\sigma}, \tag{4}$$

where α is a nondimensional constant varying between 0.2 and 0.6. In our modeling approach, we couple equation (3) with equation (4) to take into consideration the reduction of the effective stress effect resulting from the increase of pore pressure after fluid injection:

$$\dot{\theta} = 1 - \frac{V\theta}{d_c(x)} - \frac{\alpha\theta}{b(x)\sigma_{\text{eff}}}\dot{\sigma}_{\text{eff}} = 1 - \frac{V\theta}{d_c(x)} + \frac{\alpha\theta}{b(x)(\sigma_T - p)}\dot{p}. \tag{5}$$

Table 1
List of Physical Parameters

Parameter	Symbol	Value	Comment
Length of the fault	L_0	1,754.5 m	Maximum magnitude expected $M_w \approx 4$
Sliding velocity	V_0	10^{-9} m/s	Typical relative plate motion
Friction coefficient	μ_0	0.6	(Marone, 1998)
Minimum half length of asperity	R_{min}	≈ 4.84 m	Larger than the nucleation size
Maximum half length of asperity	R_{max}	≈ 167 m	
Minimum characteristic distance	$d_{c_{min}}$	0.01 mm	In agreement with values found in the laboratory (Marone, 1998)
Maximum characteristic distance	$d_{c_{max}}$	≈ 0.37 mm	In agreement with values found in the laboratory (Marone, 1998)
Characteristic distance on VS patches	d_{c_s}	0.092 mm	In agreement with values found in the laboratory (Marone, 1998)
Damping coefficient	η	5 MPa s m^{-1}	(Rice, 1993)
Rate- and State- parameters	a_w	3.10^{-4}	On VW patches
	a_s	$7.2.10^{-3}$	On VS patches
	b_w	7.10^{-4}	On VW patches
	b_s	$5.9.10^{-3}$	On VS patches
Ratio a/b	a_w/b_w	≈ 0.43	On VW patches
	a_s/b_s	1.2	On VS patches
Normal stress	σ	100 MPa	Approximate lithostatic stress at 3-km depth
Shear modulus	G	30 GPa	Typical for a wide range of crustal rocks, sedimentary, metamorphic or igneous (Turcotte & Schubert, 2014)
Dynamic velocity	v_{dyn}	0.006 m/s	$v_{dyn} = a\sigma/\eta$ (Rubin & Ampuero, 2005)
α coefficient	α	0.23	in the range proposed by Linker and Dietrich (1992)
Diffusivity	D	0.005 m^2/s	(Jaeger et al., 2007)
Injection pressure	p_{max}	0.5–20 MPa	Refer to section 3.3.1
Injection pressure rate	β	0.01–10 MPa/day	Refer to section 3.3.1

Note. VW = velocity weakening; VS = velocity strengthening.

We define a linear fault with a heterogeneous distribution of the rate and state constitutive parameters a and b. We propose a combination of velocity-weakening and velocity-strengthening patches along the fault, noted in the following as VW and VS, respectively. Each patch is characterized by a particular set (a, b, d_c) of rate and state parameters. The friction coefficient on the fault is governed by the the ratio $r(x) = a(x)/b(x)$. The fault exhibits a velocity weakening or velocity strengthening behavior, for r smaller or bigger than 1, respectively. While the VW patches (called "asperities") are more likely to break under seismic loading, the VS ones (called "creeping areas" or "barriers") slide aseismically most of the time. Although the effect of injection on the aseismic slip is not the purpose of this study, we considered VS as a way to increase seismic complexity. On the VW patches, $a = a_w = 3.10^{-4}$ and $b = b_w = 7.10^{-4}$, giving $r \approx 0.43$, while on the VS patches, $a = a_s = 7.2.10^{-3}$ and $b = b_s = 5.9.10^{-3}$, giving $r = 1.2$ (values from Table 1). Moreover, we consider a heterogeneous distribution of the different patch sizes. We sample 58 different patches, where the half length of the different patches is distributed following a power law with a -2 exponent (see Figure 1b). We constrain the size of the patches to always exceed the critical size $L_b = Gd_c/b\sigma$ (G is the shear modulus of the elastic medium, value in Table 1), so that the different VW patches are able to rupture seismically (Rubin & Ampuero, 2005). In this study we choose R to vary in the range [4.5–167] m. Figure 1b represents the distribution of the half length of the patches, showing $R_{min} \approx 4.84$ m and $R_{max} \approx 167$ m. The 58 samples are randomly distributed along the fault segment. We then assign for each patch a VW or VS behavior, in order to verify a density of asperity ρ of 0.7 ($\rho = L_a/L_0$, where L_a represents the VW length, that is, the summation of the lengths of the VW asperities). Figure 1c represents the distribution of the a and b parameter along the fault, while Figure 1d represents the ratio a/b. These values correspond to values found in the laboratory

(Marone, 1998). The choice of $d_c(x)$ was made as follows: It was observed that fracture energy G_f scales with slip δ (Abercrombie & Rice, 2005; Ohnaka, 2003), as follows $G_f = a\delta^\gamma$, where a and γ are constants; in the context of rate and state friction, the fracture energy is approximately proportional to the critical slip distance $G_f \propto d_c$ (Rubin & Ampuero, 2005); on the other hand, from elasticity, the slip δ is proportional to the patch size $2R$ and hence to R: $\delta \propto R$. By substituting these two relations in the fracture energy scaling law, we get a proportional relation between the critical slip distance and the patch size $d_c \propto R^\gamma$. In this study we therefore consider a heterogeneous distribution of d_c along the fault; we assume $\gamma = 1$ and propose a space-depending critical slip distance $d_c(x)$ on the VW patches defined as follows: $d_c(x) = d_{c0}R(x)/R_{\min}$, where d_{c0} is the minimum critical slip distance. The minimum and maximum values of d_c are chosen in a way to ensure that $R_{\min} > \min(L_b) = G(d_{c_{\min}})/b\sigma$, and $R_{\max} > \max(L_b) = G(d_{c_{\max}})/b\sigma$. Thus, d_c varies in the range [0.01–0.37] mm, in agreement with values found in the laboratory (Marone, 1998). On the other hand, d_c on the VS patches is considered constant noted d_{cs}, its value was chosen to ensure a good discretization of the VS patches, which will be discussed later. Figure 1c represents the distribution of d_c along strike of the fault, while in Figure 1d we can compare the values of R and L_b along strike of the fault. This approach involving a heterogeneous distribution of patch sizes along with scale-dependent d_c (on fracture energy) was originally developed by Ide and Aochi (2005) to study dynamic ruptures. One of the advantages of our numerical description is the possibility to model the entire seismic cycle and to take into consideration both the weakening and strengthening behaviors of the fault, so that one segment can be reactivated several times, and complex ruptures of multiple sizes can be generated.

We suppose a punctual injection of liquid water into the center of the fault (Figure 1a). We increase the pore pressure at the center ($x = x_c$) linearly with time from the beginning of the injection at $t = t_i$ to $t = t_r$ following a slope β to reach a certain maximum pressure $p_{\max}$, then maintain it constant until the shut-in of the fluid injection at $t = t_{\text{end}}$. We consider that the pore pressure at the injection point drops with the same injection slope β after shut in.

$$
p(x_c, t) = \begin{cases}
0 & \text{if} \quad t < t_i \\
\beta(t - t_i) & \text{if} \quad t_i < t < t_r \\
\beta(t_r - t_i) = p_{\max} & \text{if} \quad t > t_r \\
p_{\max} - \beta(t - t_{\text{end}}) & \text{if} \quad t > t_{\text{end}}
\end{cases} \tag{6}
$$

We allow the fluid to diffuse along the fault segment, following the 1-D diffusion equation:

$$
\frac{\partial p(x, t)}{\partial t} = D \frac{\partial^2 p(x, t)}{\partial x^2}, \tag{7}
$$

where $p(x, t)$ is the pore pressure and D is the homogeneous diffusion coefficient defined as $D = K/(\phi\mu c)$, where K is the permeability, ϕ is the porosity, μ is the viscosity and c is the summation of the pore fluid compressibility and the compressibility of pore volume due to pore pressure changes (Jaeger et al., 2007). In this study we use typical values for those parameters giving $D = 0.005$ m²/s (value in Table 1; Jaeger et al., 2007). Even though, it was observed that hydromechanical and frictional properties of the fault are coupled (Ikari et al., 2009), for simplicity we neglect this effect and we consider only the direct changes in pore pressure on the rate and magnitude of induced events. We assume that the simulations are isothermal and there is no chemical interaction between the liquid water and the rocks. At first, we assume Dirichlet boundary conditions and impose zero pressure at the edges of the finite fault segment. Other boundary conditions (Neuman) were tested and are discussed in the following section.

Finally, the far-field stressing and the heterogeneous slip distribution along the fault generate elastic stresses that could be approximated by the quasi-dynamic stress τ_e

$$
\tau_e(x, t) = \frac{G}{2\pi} \int_{-\infty}^{+\infty} \frac{\delta'(s, t)}{s - x} ds - \eta v(x, t), \tag{8}
$$

where G is the shear modulus of the elastic medium, δ' is the slip gradient and η is the damping coefficient ($\eta = G/2c_s$, where c_s is the shear wave velocity; Rice, 1993; see Table 1 for values of G and η).

We assume that the frictional stress (equation (2)) balances the quasi-dynamic elastic stress (equation (8)). This balance, along with the state evolution law (equation (5)), the injection (equation (6)), and the diffusion
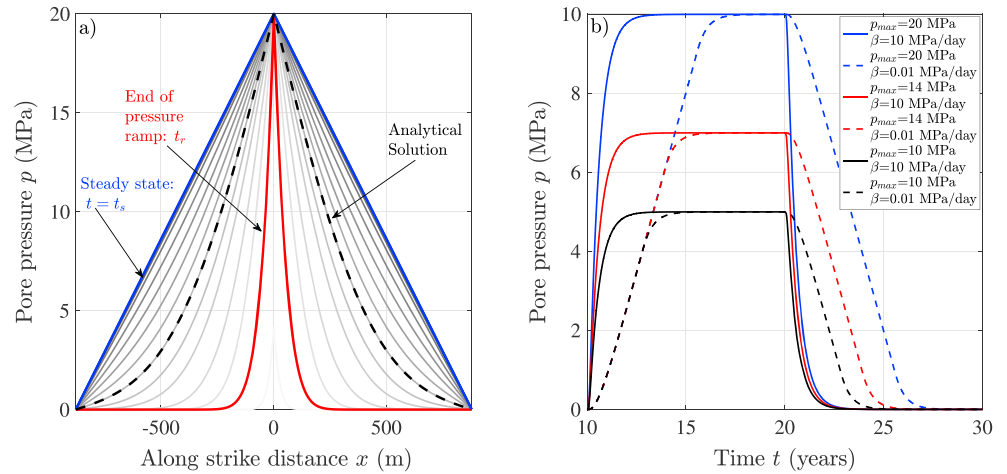
Figure 2. (a) Evolution of the pore pressure profile along strike distance with time for one injection case ($p_{\max} = 20$ MPa and $\beta = 2$ MPa/day). Darker colors correspond to later times. The red and blue curves represent the pore pressure profile at $t = t_r$ and $t = t_s$, respectively. The dashed black line represents the pore pressure profile at $t = 0.4$ years after injection calculated using the analytical solution from Appendix A. (b) Evolution of the pressure at the point ($x = 438$ m $\approx L_0/4$) with time.

equation (equation (7)) form a set of differential equations for the evolution of V, θ, and p along the fault. The system is solved using a fifth-order adaptative time step Runge-Kutta algorithm (Fehlberg, 1969). We use the method proposed by Cochard and Rice (1997) to estimate the Hilbert transform of the slip gradient at each time step and thus solve equation (8). The fault is discretized into a set of $n = 2^{11} = 2,048$ equal computational cells of size Δx. To ensure continuity, Δx should be smaller than the characteristic size $L_b = G d_c / b \sigma$ (Rubin & Ampuero, 2005). Since L_b depends of d_c which in turn is variable along the fault, then Δx should be smaller than the smallest L_b. Here we chose $\Delta x = 0.857$ m, giving $\Delta x / \min(L_b) = 0.2$ in all the computations, which is sufficient to ensure continuity. We also force Δx to be smaller than $L_{bs}/5 = G d_{cs}/5 b_s \sigma$ to ensure a good discretization on the VS patches. To satisfy this condition d_{c_s} should be larger than $5 \Delta x b_s \sigma / G$. Here we chose $d_{c_s} = 1.1 * 5 \Delta x b_s \sigma / G = 0.092$ mm. Figure 1d represents the distribution of L_b along the fault, along with the chosen Δx. We use the FTCS (forward difference approximation in time and a central difference approximation in space) explicit finite difference scheme to solve the diffusion equation, using the same spatial discretization. A sufficient criterion for the stability of the numerical resolution of the finite difference scheme is expressed as a condition on the time step Δt:

$$\Delta t \leq \frac{\Delta x^2}{2D}. \tag{9}$$

At each iteration, the time step estimated by the Runge-Kutta algorithm is checked against the stability condition (equation (9)).

For initial conditions, we imposed steady state $V = V_0$ and $\theta = \theta_0 = d_{c0}/V_0$ over the VS areas, and we assumed a random distribution of velocity and state variable for the VW patches, where $\log_{10} V_0$ and $\log_{10} \theta_0$ are uniformly distributed between $[-19, -8]$ m/s and $[3, 4]$ s^{-1}, respectively. We let the fault evolve for several cycles while it loses the memory of the initial conditions, before studying the effect of fluid injection. In all the simulations presented below, injection starts at $t = 10$ years and ends at $t = 20$ years. Features of seismic activity before injection starts will be discussed in the next section. Figure 2a shows an example of the evolution of the pore pressure profile along strike. In this example, the pressure at the edges of the fault segment is assumed to be 0 (Dirichlet boundary conditions). At first a transient state governs, where the pressure at the center increases and then stabilizes, while the pore pressure diffuses along strike. After some time, a steady state is reached. In the following, this time is noted t_s. The pressure distribution has been validated by comparison with an analytical solution (see Appendix A). In this figure, the black dashed line represents the pressure profile for $t = 0.4$ years after injection starts, estimated using equation (A2). Figure 2b shows the effect of the injection parameters β and $p_{\max}$ on the evolution of the pressure at one point ($x = 438$ m $\approx L_0/4$) with time. Different values of $p_{\max}$ are represented by different colors, while two different values of β are presented by different line styles.

When the maximum slip rate exceeds a threshold velocity $v_{\text{dyn}} = a\sigma/\eta$ (Rubin & Ampuero, 2005), the radiation damping term becomes greater than the direct effect of rate- and state-dependent friction. In this case, the elastodynamic effects governs the system. We use this criteria to detect the earthquake onset and thus to create an earthquake catalog for each simulation. Following each event, we estimate a rupture size L, and we compute the cumulative seismic moment released according to

$$M = GS < \delta >, \tag{10}$$

where S is the surface of the rupture and $< \delta >$ is the average slip. Since the model is 2-D, we use an equivalent rupture surface S defined as $\pi L^2/4$. The average slip is computed as

$$< \delta > = \frac{1}{L} \int_{-L/2}^{L/2} (\delta(x, t_2) - \delta(x, t_1)) \mathrm{d}x, \tag{11}$$

with t_1 and t_2 the onset and the end time of the earthquake. Thus, the seismic moment would be

$$M = \frac{\pi GL}{4} \int_{-L/2}^{L/2} (\delta(x, t_2) - \delta(x, t_1)) \mathrm{d}x. \tag{12}$$

Then, we estimate the moment magnitude M_w using the expression given by Hanks and Kanamori (1979):

$$M_w = \frac{2}{3} \log_{10}(M) - 6.06, \tag{13}$$

where M in expressed in Newton meters.

The physical parameters used in the next sections are presented in Table 1.

3. Results

3.1. Background Seismicity

Our main objective is to study the effect of fluid injection on the features of seismic activity. The features of seismic activity along the fault during 10 years before fluid injection are presented in Figures 3a1, 3b1, 3c, and 3f. Figure 3a1 gives an idea about the time series of the moment magnitude and its mean value estimated using a centered sliding average, with a sliding window of 50 events. The proposed fault model can produce earthquakes of different moment magnitudes M_w in the range [0–3.5]. The cumulative number of earthquakes and the cumulative seismic moment released increase quasi-linearly in time, with an average of 170 earthquakes and $2.3.10^{14}$ N m of seismic moment released per year (see Figure 3b1). In the following sections, we will note S_0 the seismicity rate before injection (equal to 170 earthquakes per year) and M_0 the moment rate before injection (equal to $2.3.10^{14}$ N m/year). Figure 3c presents slip profiles for a sequence of 50 successive earthquakes before fluid injection, along with the distribution of the frictional ratio a/b so that we can differentiate VW and VS patches. We can observe a complex pattern of seismic ruptures separated by slow aseismic slip episodes (represented by the area hatched by light cyan in the plot). There exist some small ruptures localized on the smaller VW patches (for instance event A). In this case, the neighboring VS barrier stops the propagation of the rupture along strike. However, along the bigger VW patches, the ruptures are larger and can go beyond the neighboring VS barriers (for instance event B). The proposed fault model can hence generate a complex pattern of ruptures and can bear earthquakes of different magnitudes following a Gutenberg Richter distribution with slope $b \approx 1$ (see Figure 3f).

3.2. Response to Fluid Injection

Figures 3a2, 3b2, and 3d–3f represent the different features of seismic activity after fluid injection started for the case study with the following injection parameters $p_{\max} = 20$ MPa and $\beta = 2$ MPa/day (injection scenario presented in Figure 2a). Figure 3a2 represents the time series of the moment magnitude M_w after injection starts; we observe clearly that fluid injection changes the distribution of the magnitude of the events. This will be further investigated in Figure 3f. After injection starts, the cumulative number of earthquakes along with the cumulative seismic moment experience an enormous increase at the very start of the injection (Figure 3b2). During the first year after the injection start, 1,450 earthquakes were detected and around 2.10^{15} N m of seismic moment was released. Once the pore pressure reaches a permanent state along the fault ($t = t_s$), the cumulative number of earthquakes seems to retake approximately its initial slope; however, the seismic moment appears to be increasing slightly slower than before injection started. At the
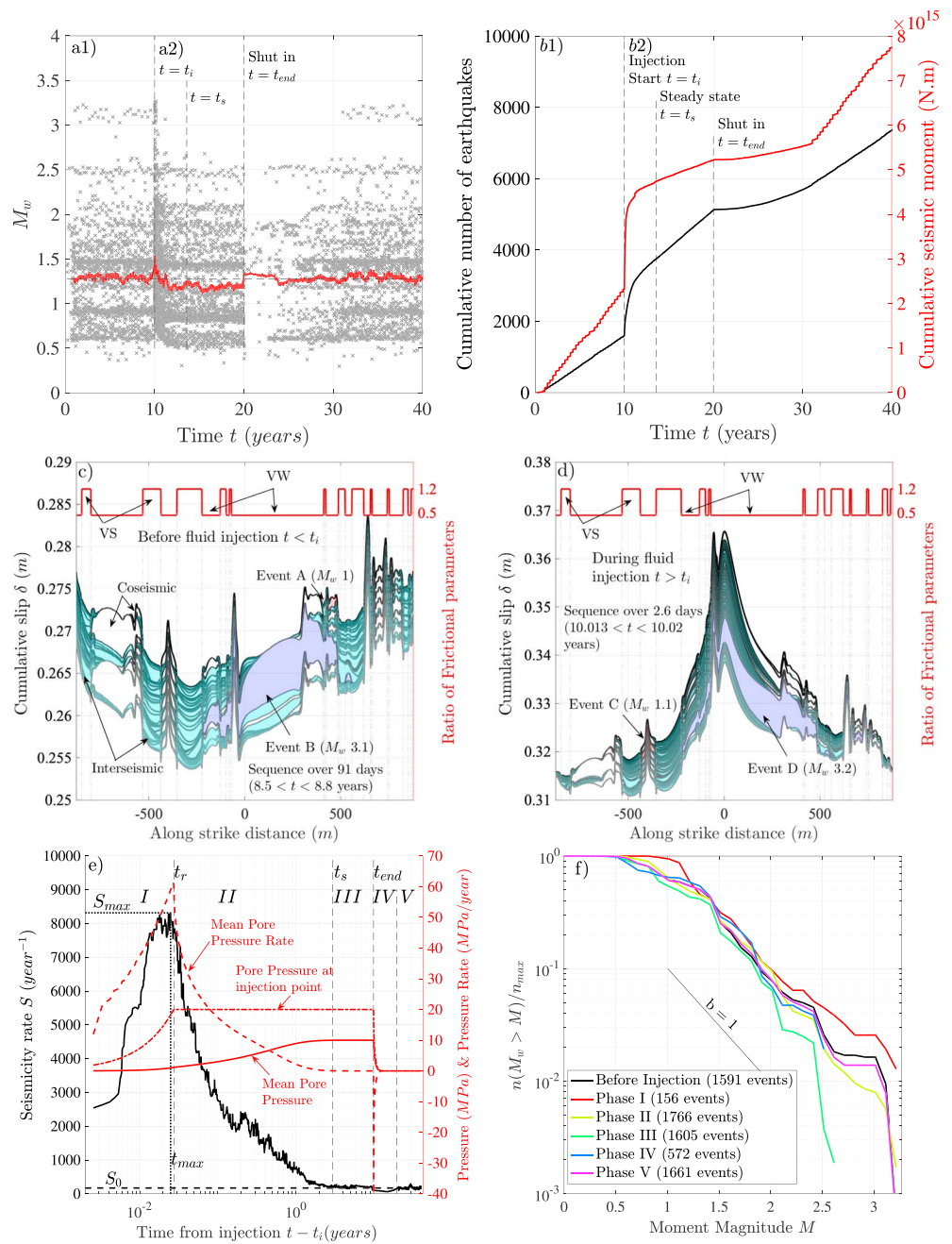
Figure 3. (a) Time series of the moment magnitude M_w. The red curve is a centered sliding average, with a sliding window of 50 events. The horizontal dashed line is the mean value of M_w. (b) Cumulative number of earthquakes (black curve) and seismic moment in Newton meters (red curve). (c, d) Example of the cumulative slip profiles along strike distance for a consecutive 50 earthquakes: One profile is represented before and after each earthquake. (White, blue, and red areas are the coseismic offsets of earthquakes, and light cyan represents the aseismic slip accumulated during the interseismic periods.) Darker colors represent later times. The red curve represents the ratio of frictional parameters a/b along strike distance. (e) Time series of the seismicity rate (black curve), mean pore pressure, pore pressure at injection point, and mean pore pressure rate, on a semilogarithmic scale. The black horizontal dashed line represents the initial seismicity rate S_0 (before injection). Dotted lines represent the point (t_{max}, S_{max}), where the seismicity rate reaches its maximum. The time axis is normalized from the injection start time t_i. (f) Magnitude frequency distribution of the events before (black curve) and in the different phases (colored curves).

injection shut in (10 years after the injection started), seismic activity slows down, in terms of number of earthquakes and seismic moment, for around 12 years, before gaining its initial preinjection activity. Figure S1 (from the supporting information) represents the time series of the moment magnitude, while Figure S2 represents the cumulative number of earthquakes along with the cumulative seismic moment release, for different injection scenarios, where we can see that the results for the different cases present the same trend as the observations made for the case studied here. Note that the slowing moment increase in Phase III is particularly evident for $p_{\max} > 10$ MPa. This issue will be discussed later. As for the slip distribution along the fault, from Figure 3d, we can still observe a complex pattern of seismic ruptures with small localized ruptures on VW patches (event C for instance) and large ones on VW and VS patches (event D for instance). However, we also can observe a large slip concentration at the center of the fault, around the injection point where the pressure perturbation is the largest. The slip at the center of the fault is larger by around 13%.

In order to better quantify the changes in seismic activity in terms of number of earthquakes, we estimated the seismicity rate (gradient of the cumulative number of events with respect to time). Figure 3e illustrates the time evolution of the seismicity rate, the mean pore pressure, and the mean pore pressure rate, during fluid injection and after shut in. In order to avoid numerical peaks and oscillations, the seismicity rate was smoothed, using a moving median filter with a nonconstant sliding time window of width the length between 20 consecutive events. We can clearly discern three different phases during fluid injection and two after injection shut in: (I): $t_i < t < t_r$, where the pore pressure increases linearly at the injection point, (II): $t_r < t < t_s$ where the pore pressure at the injection point is maintained constant (equal to $p_{\max}$) but the pore pressure is not at steady state yet, (III): $t_s < t < t_{\mathrm{end}}$, where t_s is the time needed by the pore pressure profile, along the fault, to reach a permanent state, (IV): $t > t_{\mathrm{end}}$, where the pressure at the injection point drops and (V): when all the pore pressure is diffused outside the fault. During Phase I, the mean pore pressure and the mean pore pressure rate increase along the fault leading to an increase of the seismicity rate, whereas in Phase II, while the mean pore pressure keeps on increasing, the seismicity rate decreases along with the mean pore pressure rate. Finally, in Phase III, the mean pore pressure is constant, the pore pressure rate drops to 0, and the seismicity rate stabilizes around the initial preinjection seismicity rate S_0, presented by the dashed horizontal line. Additionally, the peak in the seismicity rate approximately coincides with the peak in pore pressure rate, both at $t = t_r$. Phase IV starts at the injection shut in. In this phase, the pore pressure drops, the pore pressure rate takes negative values, and the seismicity rate is lower than S_0 for around 12 years. Finally in Phase V, the pore pressure and the pore pressure rate are 0, and the seismicity rate regains its initial value S_0 one more time. According to these results, the seismicity rate seems to follow the evolution of the pore pressure rate, rather than the pore pressure itself. As illustrated in Figure S3 (supporting information), this correlation is obtained for almost all the injection scenarios tested. For large β and small $p_{\max}$, the evolution of the seismicity rate is slightly delayed with respect to the pore pressure rate. For the other cases, we observe a direct correlation between the time series of both the seismicity rate and the pore pressure rate.

Figure 3f represents the evolution of the magnitude-frequency distribution of the events throughout this case study before injection (black curve) and for the different phases (colored curves). Before fluid injection, the magnitudes of the events follow a power law distribution between $M_w = 0.5$ and around $M_w = 3.2$ with a b value close to 1. Due to fluid injection, the magnitude-frequency distribution changes. To start, it appears that Phase I is the most critical: The frequency of intermediate and large magnitudes ($M_w \geq 1.5$) are increased (please note that the used terms intermediate and large are relative to the magnitude range that we have in our results here). This is also observed by the rapid increase of the mean of M_w directly after injection start in Figure 3a2. In Phase II, however, we observe a decrease in the frequency of larger magnitudes ($2.2 \leq M_w \leq 3.2$), relative to Phase I. This suggests that the effect of β which only acts in Phase I and $p_{\max}$ which acts in both Phases I and II are not the same. This feature will be further investigated in the next section. In Phase III, the magnitude-frequency distribution is perturbed as well, even though there is no more amplification of the seismicity rate. In this period we observe from Figure 3f a deficit of the magnitudes in the range $0.7 \leq M_w \leq 2.6$, absence of very large magnitudes ($M_w \geq 2.6$) and re-apparition of the small magnitudes (better observed in Figure 3a2), which explains the slow increase of cumulative seismic moment observed in this phase in Figure 3b2. On the other hand, in Phase IV and after the shut in, we observe absence of the large magnitudes $M_w \geq 2.5$. Finally, in Phase V the magnitude distribution is quasi-similar to the preinjection one. Interestingly, in both Phases III and V, the seismicity rate is the same (equal to S_0) and the pore pressure rate is 0. The only difference between these two phases is the value of the
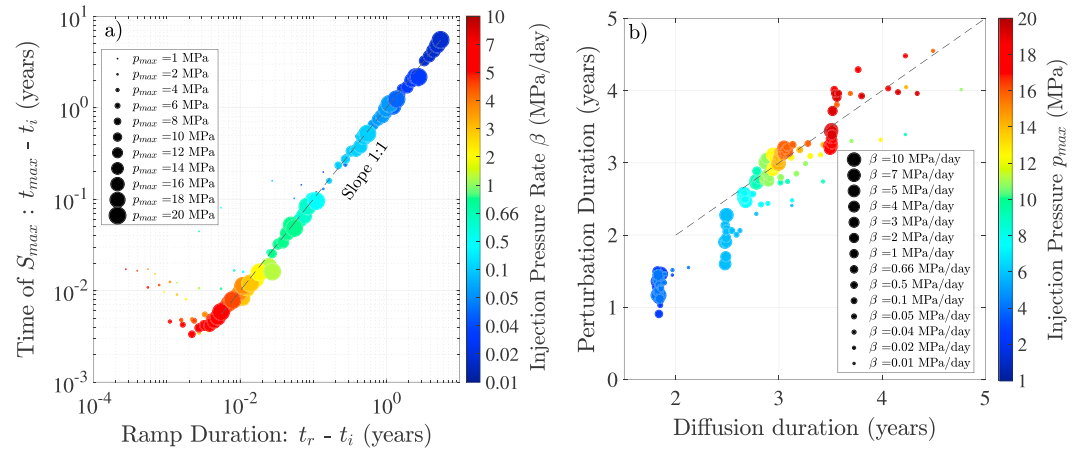
Figure 4. Influence of injection on the induced seismicity parameters: (a) Comparison of the time needed to reach the maximum seismicity rate: t_{max} and the time needed to reach p_{max} at the injection point: t_r. The color scale represents different values of the pore pressure rate β at the injection point, and the size of the scattered points is proportional to the maximum pore pressure at the injection point p_{max}. (b) Comparison of the duration of the induced seismicity sequence with the duration of fluid diffusion. Here, the color scale represents different values of the injection pressure p_{max}, and the size of the scattered points is proportional to the pore pressure rate at the injection point β.

effective stress. We have that $\sigma_{\text{eff}} = \sigma - p$, if we take the mean pressure along the fault, this would give us an effective stress of 90 MPa in Phase III where $p = 10$ MPa; in Phase V, however, $p = 0$, and the effective stress would be 100 MPa. This suggests that the reduction of the effective stress in Phase III may be the cause of the perturbation of the magnitude distribution. We should note that in this case study the maximum magnitude was not exceeded during fluid injection, we will show however in the next section that this may not be the case for different values of β.

3.3. Sensitivity Analysis

In the following, we study the effect of the injection parameters on the seismicity rate and the magnitude distribution. We concentrate on Phases I and II where seismicity increases. We do not investigate further Phase IV because our model is not adapted to study postinjection seismicity, which could be attributed to neighboring faults. This will be discussed later.

3.3.1. Choice of Injection Parameters

One hundred sixty-eight injection scenarios were tested by varying independently both the injection pore pressure p_{max} and the injection pressure rate β, with a constant diffusivity D and dirichlet diffusive boundary conditions. Twelve different values of p_{max} are tested in the range [0.5–20] MPa = $[0.005–0.2]\sigma_T$. This yields a local reduction of the effective stress between 0.5% and 20% at the injection point, and between 0.25% and 10% globally along the fault (if we assume a mean pressure along the fault). On the other hand, we tested 14 different values of the injection pressure rate β in the range [0.01–10] MPa/day. This range of values was chosen in order to cover a wide domain of the ratio of injection rate to background rate $(\dot{\tau}_{\text{inj}}/\dot{\tau}_0)$. We estimate the injection stressing rate $\dot{\tau}_{\text{inj}}$ during Phase I at the injection point : $\dot{\tau}_{\text{inj}} \approx (\mu_0 - \alpha)\dot{p} = (\mu_0 - \alpha)\beta$, since at the injection point $\dot{p} = \beta$ and because rate and state friction coefficient is only a small correction to a constant friction coefficient μ_0. This yields $\dot{\tau}_{\text{inj}}$ to vary in the following domain [0.043–43] Pa/s. On the other hand, we estimate an approximate background stressing rate $\dot{\tau}_0 = 0.05$ Pa/s (see Appendix B for details). Thus, for the different injection pressure rates chosen $(\dot{\tau}_{\text{inj}}/\dot{\tau}_0)$ vary in the range [0.86–860].

3.3.2. Time of Maximum Seismicity Rate and Seismicity Perturbation Duration

We should mention that in this section and for Figure 4 we will not present the results of the simulations with $p_{max} = 0.5$ MPa; the reason will be discussed in the next section. Figure 4a shows the correlation between the duration of the injection pressure slope $t_r - t_i$ (i.e., duration of Phase I) and the time delay to reach the maximum seismicity $t(S_{max}) - t_i = t_{max} - t_i$ (see Figure 3e). t_{max} depends strongly on the injection pressure rate β. Generally maximum in seismicity is reached when the pore pressure rate reaches its maximum $t_{max} \approx t_r$. However, for very small values of injection pressure p_{max} or for the combination large values of β with intermediate values of p_{max}, Phase I is really short and the seismicity rate can continue to increase for an additional time beyond Phase I: $t_{max} > t_r$, illustrated in Figure S3 as well.
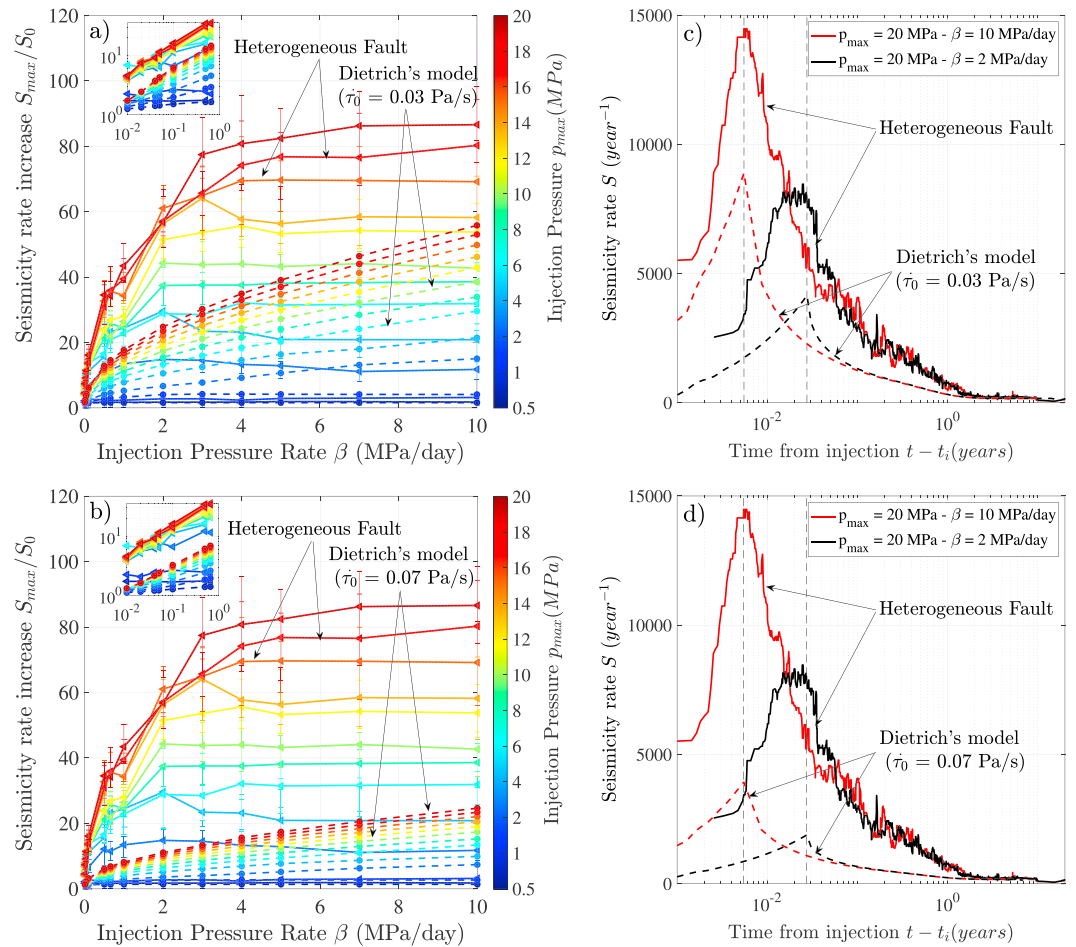
Figure 5. (a, b) Seismicity rate increase $S_{\max}/S_0$ (ratio of maximum seismicity rate over seismicity rate before injection) as a function of the injection pore pressure rate β. Continuous lines represent the results of the numerical model of the heterogeneous fault; dashed lines represent the seismicity rate increase predicted by analytical approximation based on Dietrich's 1994 model (for $\dot{\tau_0} = 0.03$ in subplot a and 0.07 Pa/s in subplot b). Error bars represent the variability of $S_{\max}/S_0$ for one simulation. The color scale represents different values of the maximum injection pressure $p_{\max}$. The small subplot inside the figure is a zoom of the results over the small range of β ($\beta <$ 1 MPa/day). (c, d) Time series of the seismicity rate for two different injection scenarios. Continuous lines represent the numerical seismicity rate, and dashed lines represent the one predicted by Dietrich's model (for $\dot{\tau_0} = 0.03$ in subplot c and 0.07 Pa/s in subplot d). The vertical dashed lines represent the time t_r for the different injection scenarios.

Figure 4b shows the correlation between the diffusion duration and the seismicity perturbation duration. The diffusion duration is the duration for the pore pressure to reach a permanent state along the fault $t_s - t_i$, and the seismicity perturbation duration is picked manually for the different simulations as the time when the seismicity rate regains its initial value S_0. For larger $p_{\max}$, the time to reach a permanent state is larger, and hence we would expect a larger diffusion duration. From the results, we observe a clear correlation between the duration of the seismicity perturbation and the diffusion duration with a dependence on the injection pressure $p_{\max}$. However, for low values of $p_{\max}$, the perturbation duration seems shorter than the diffusion duration, because in this case, the pressure perturbation along strike of the fault near the end of the diffusion is very small relatively to other cases, and thus this may cause the seismicity perturbation to cease. These results suggest that for the different injection scenarios considered, the seismicity perturbation is generally governed by the diffusion of the fluid along the fault segment, thus by the evolution of the pore pressure rate along the fault, once a permanent state for pressure is reached, it will lead to a constant seismicity rate.

3.3.3. Seismicity Rate Increase

In order to compare the different cases, we quantified the seismicity rate increase due to fluid injection for each case as follows: $S_{\max}/S_0$, where $S_{\max}$ is the maximum seismicity rate and S_0 is the initial seismicity rate before injection (see Figure 3e). The evolution of the seismicity rate increase with both β and $p_{\max}$ is

represented in Figure 5a. The small subplot inside the figure is a zoom of the results over the small range of β ($\beta < 1$ MPa/day). First for the lowest value of p_{max} (0.5 MPa) we do not observe any significant increase in the seismicity rate no matter the value of β. That is why the results of these simulations were not taken into account in the previous section, nor will they be taken for the rest of the study. For $p_{max} = 1$ MPa, however, we observe a slight increase in the seismicity rate with no dependence on β. For $p_{max} \geq 2$ MPa, S_{max}/S_0 increases quasi-linearly with the injection pressure rate β until a certain threshold β^*. Beyond it, the seismicity rate increase shows almost no evolution. This rate threshold β^* however is not the same for the different values of p_{max}, it appears to be pressure dependent, and take larger values for larger p_{max}. For example, we reach a stable S_{max}/S_0 for $\beta \geq 3$, 2, and 1 MPa/day for $p_{max} = 20$, 14, and 4 MPa, respectively. The seismicity rate increase S_{max}/S_0 increases also with increasing injection pressure p_{max}; however, the dependency on p_{max} is much less pronounced for very small values of β. The seismicity rate could be increased up to a factor 80.

Dietrich (1994) proposed an analytical model for the seismicity rate following stress perturbations, with rate- and state-dependent fault properties. He modelled a population of identical asperities as rate and state spring slider systems. Similarly, we can apply Dietrich's assumptions to our fault configuration, and assume that the fault is made of a collection of independent and noninteracting spring slider systems. We can then compute the seismicity rate predicted by Dietrich's model. Details about the procedure are provided in Appendix C, we should note though that we used the two values of $\dot{\tau}_0$ (0.03 and 0.07 Pa/s) estimated in Appendix B. In Dietrich's model, the different asperities are identical and independent in the sense that no stress transfer is allowed between them. The resulting events would have the same magnitude, that is proportional to the size of the asperity; thus, by choosing the number of asperities, we choose the resulting magnitude of the events as well. In order to cover the M_w range observed in our model, we tested different values of the number of asperities used in the range $[L_0/R_{max}-L_0/R_{min}] \approx [10–350]$ asperities, so that in any case we would not have larger or smaller asperities than the ones used in our model. Beyond a certain number of asperities, this model converges and gives the same estimation independently from the number of asperities chosen. We present here the results for a case with 100 asperities, where the size of the different patches is $\approx R_{max}/10$. The estimations of the seismicity rate increase based on this model for every combination of injection parameters (p_{max}, β) are presented in Figures 5a and 5b by the dashed lines (for $\dot{\tau}_0 = 0.03$ and 0.07 Pa/s, respectively). First we observe that the results depends on $\dot{\tau}_0$, where a lower background stressing rate, thus a higher ratio $\dot{\tau}_{inj}/\dot{\tau}_0$ can lead to a larger seismicity rate increase. Thus, we cannot rely totally on the estimation of the seismicity rate increase that we make from this model, however it can give us a good idea of its quantification with respect to our numerical results. Generally, Dietrich's (1994) seismicity rate increase presents the same trend as the numerical one: We observe a similar dependency with the injection pressure p_{max}, and we also observe that the seismicity rate increases with β. For low values of p_{max}, the seismicity rate increase appears to saturate when β is large. We also observe approximately no amplification on the seismicity rate for the smallest injection pressure ($p_{max} = 0.5$ MPa). However, this model underestimates the seismicity rate increase generated by our heterogeneous fault, and for $\beta > \beta^*$, the seismicity rate does not saturate, but rather keeps on increasing. In the following, we look into more details into the time series of the seismicity rate. Figures 5c and 5d represent the comparison for the time series of the seismicity rate generated by our model and the one predicted by Dietrich's model for two different injection scenarios. We can observe that generally the seismicity rate follows the same trend, it increases at the start until the time $t = t_r$, and then decreases until regaining the initial seismicity rate value. Again, we observe that the analytical approximation underestimates the seismicity rate. Finally we should note that the comparison between the two models remains limited, since Dietrich's model fails to generate a variation in earthquake magnitude, and neglects the stress transfers between the different asperities. This comparison will be further developed in the discussion section.

3.3.4. Magnitude Content

We are interested to study the effect of the injection parameters on the magnitude frequency distribution when the seismicity rate is the most perturbed, hence in the first and the second phase (see Figure 3). Since β only acts in Phase I, we are only interested to study its effect in this phase, we will however study the effect of p_{max} on both Phases I and II. Figure 6 illustrates the distribution of the moment magnitude of the events during injection, in comparison with the distribution before fluid injection (black curve, in the different subplots). Figures 6a–6c emphasize on the dependency of the magnitude distribution on the injection pressure rate β for three different values of p_{max} in Phase I, whereas Figures 6d–6f and 6g–6i emphasize on the effect of the injection pressure p_{max}, for three different values of injection pressure rate β, in Phases I and II, respectively. First, from Figures 6a–6c we observe a dependency of the magnitude frequency distribution on
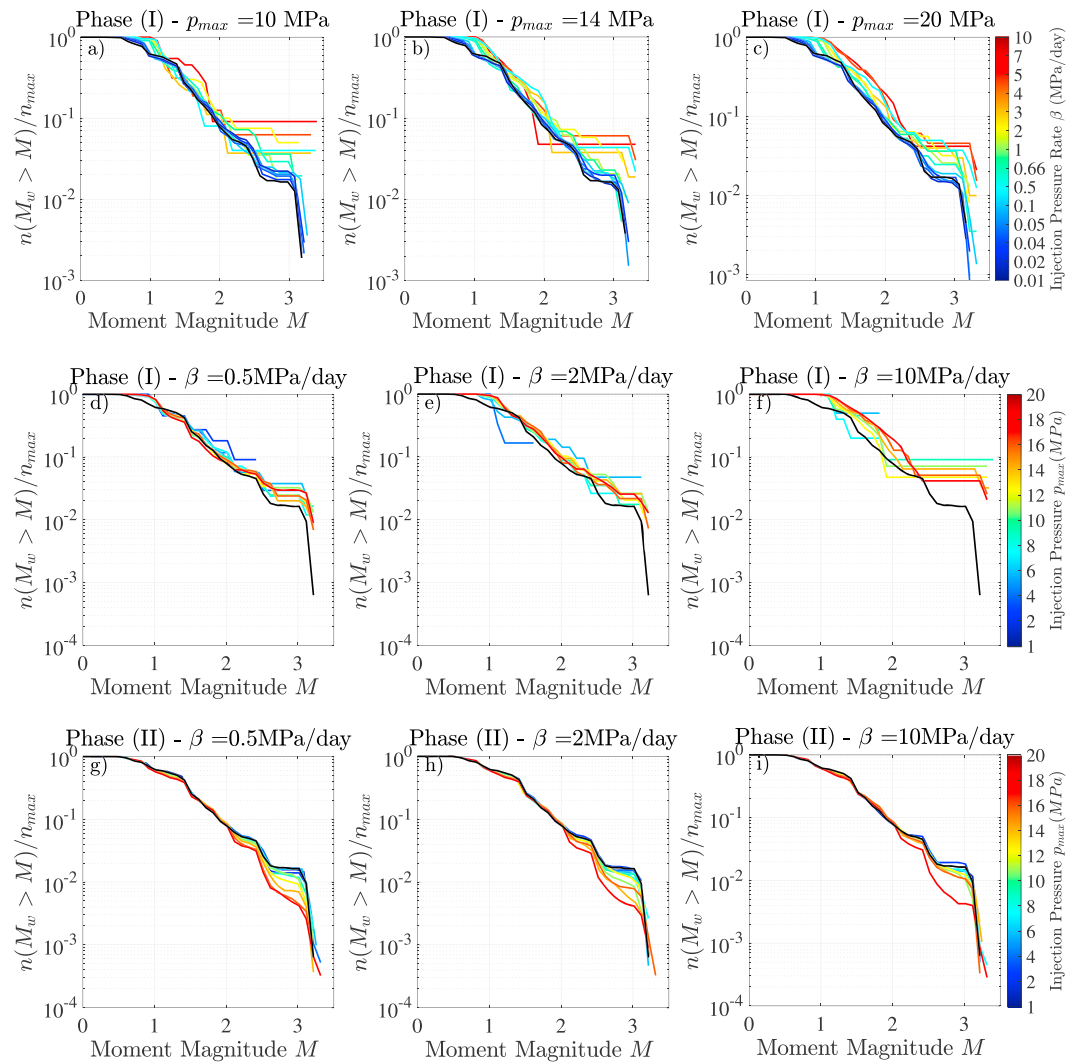
Figure 6. Moment magnitude distribution. Subplots (a)–(c) represent the magnitude distributions during Phase I for three different fixed values of p_{max}, the color scale represents the injection pore pressure rate β. Subplots (d)–(f) and (g)–(i) represent the magnitude distributions for three different fixed values of β, in Phases I and II, respectively. The color scale represents the injection pore pressure p_{max}. In all subplots, the black curve represents the moment magnitude distribution before fluid injection. n_{max} designs the total number of earthquakes in the studied time duration, and M designs the moment magnitude M_w.

the injection pressure rate β, where a larger β can produce more numerous large magnitudes ($M_w > 2$). We can also observe that the maximum magnitude $M_w \approx 3.2$ can be slightly exceeded when β is large enough, with the apparition of M_w 3.4 events (see also Figure S1). On the other hand, we do not observe a very clear dependency of the magnitude distribution on p_{max} in Phase I (Figures 6d–6f), maybe because in this phase the effect of β dominates. The dependency on p_{max} is however clear in Phase II (Figures 6g–6i). For larger pressure perturbations, we observe a more important deficit of large magnitudes ($M_w \geq 2$), whereas for small p_{max} we do not observe a significant change in the magnitude frequency distribution with respect to the one before injection. This would explain why we observed a slow moment increase in Phase III particularly for large p_{max} (see Figure S2). We observe nonetheless, a creation of slightly larger magnitudes in Phase II as well.

To better quantify the magnitude changes, we estimate the b value using the maximum likelihood method (Aki, 1965), in the following range [1–3.2] separately for Phases I and II. $M_w = 1$ is approximately the completeness magnitude of our catalogue (see Figure 6). However, for Phase I we only consider the simulations where this phase is large enough in time so the fault has time to generate enough earthquakes (here we chose
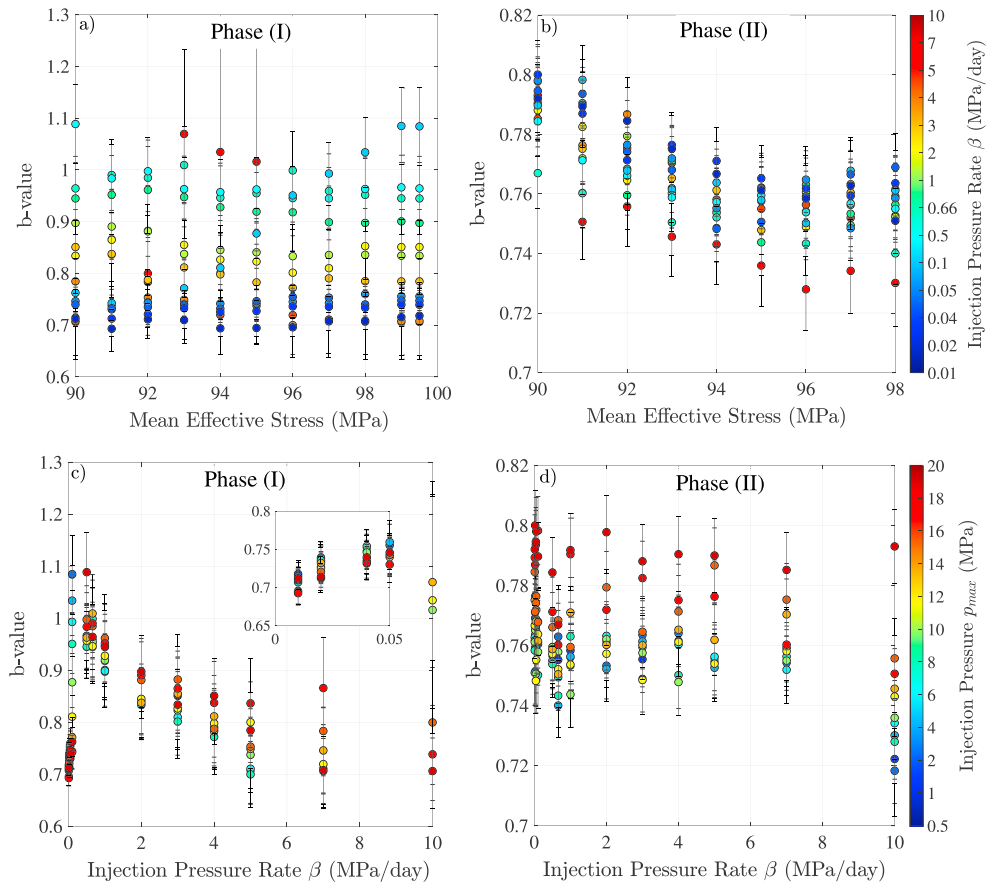
Figure 7. Evolution of the b value, estimated in the M_w range [1–3.2], with the change in effective stress in (a) Phase I and (b) Phase II. The color scale represents different values of injection pressure rate β; and with β in (c) Phase I and (d) Phase II. The small subplot in (c) is a zoom over the small range of $\beta \leq 0.05$ MPa/day. The color scale represents different values of injection pressure $p_{\max}$. Error bars represent the error on the estimation of the b value for one simulation.

a minimum of 50 earthquakes to perform the b value computation) in this period to have a good estimate of the b value, otherwise the b value would be biased and its variability would be large. The standard errors were evaluated following Shi and Bolt (1982). Results of the b value are evaluated with respect to changes to the mean effective stress along the fault ($< \sigma_{\mathrm{eff}} > \approx \sigma_T - p_{\max}/2$) in Figures 7a and 7b, and with respect to changes in β in Figure 7c and 7d. During Phase I, the b value depends especially on the value of β (Figure 7c) and does not vary significantly with the effective stress hence with $p_{\max}$ (Figure 7a). For small values of $\beta \leq 0.05$ MPa/day, the b value increases with increasing β, which could be attributed to an increase in the magnitude of completeness from $M_w = 0.5$ to $M_w = 1$ observed in Figures 6a–6c. Beyond 0.05 MPa/day, we observe a decrease of the b value with increasing β, which suggests an increase in the proportion of large magnitudes in the studied range. However, for very large β, the uncertainty in the b value is important. This reflects the deviation from a power law decay for large β illustrated in Figures 6a–6c. On the other hand, in Phase II, from Figures 7b–7d we observe that the b value tends to decrease with increasing the mean effective stress, with no clear effect of β in this period, which makes sense because β only acts in Phase I.

3.3.5. Seismic Moment Release and Number of Earthquakes During Phase I, Phase II, and Phase (I–II)

From the previous analysis made on the seismicity rate and magnitude content during Phase I, it appears that there is simultaneous saturation of the maximum seismicity rate, increase of the proportion of large M_w and a decrease of the b value as β increases. Moreover we observed that during Phase II, $p_{\max}$ has an important effect on the magnitude distribution and the b value. However, it was hard to make the correlation directly between the seismicity rate increase and the change in the b value. This is because a change in the b value can be interpreted in different ways, for instance in our study we can observe a decrease of
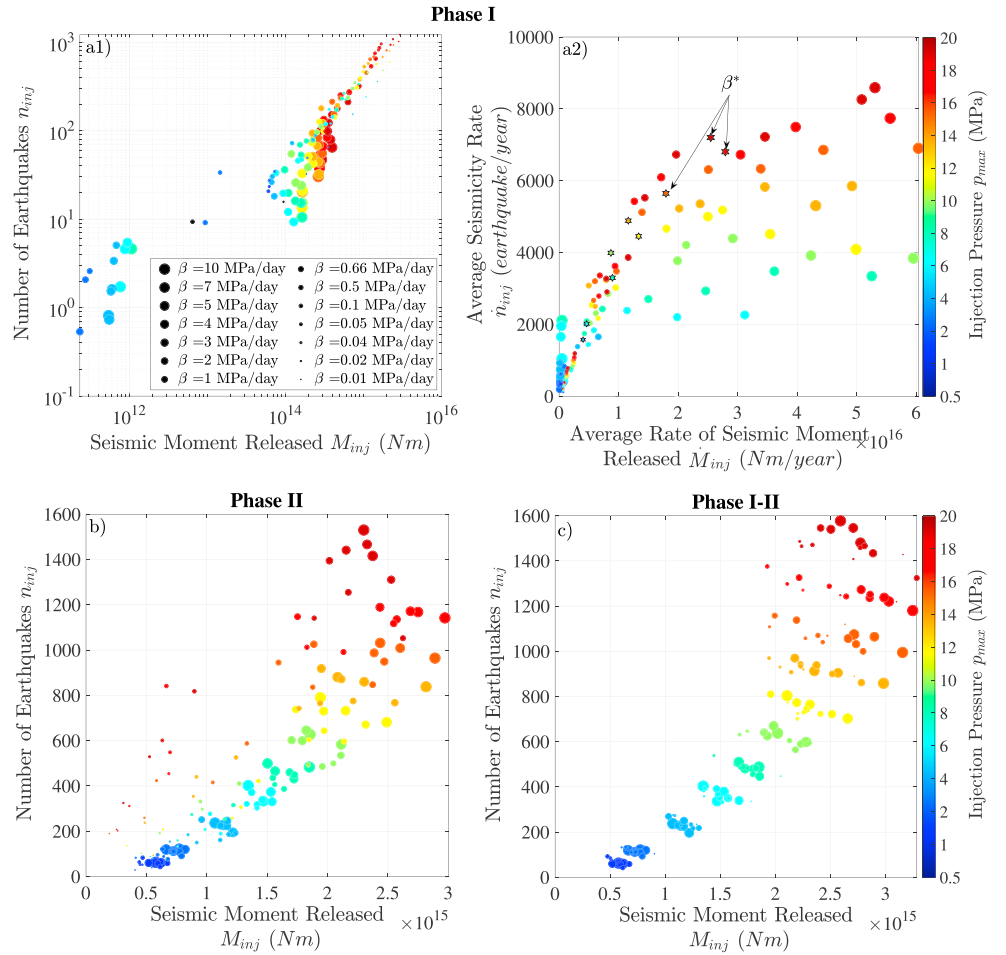
Figure 8. (a1, b, c) Evolution of the number of earthquakes and the seismic moment released with the injection parameters, in Phase I, Phase II, and Phase I + II, respectively. (a2) Evolution of the average seismicity rate and the average seismic moment rate with the injection parameters in Phase I. In this subplot, the different stars represent the values of β^*; each color refers to a p_{max}. In all subplots the color scale represents the injection maximum pressure p_{max}, and the size of the scattered points represents the injection pressure rate β.

the b value by either only increasing the frequency of the largest magnitudes, or by creating new larger magnitudes, or by decreasing the frequency of the smallest magnitudes. Thus, to better understand the link between the seismicity rate and the magnitude distribution for the different injection scenarios, we looked into the changes in the cumulative seismic moment released and the number of earthquakes, due to fluid injection, in Phases I, II, and (I–II). In the following, we note n_{inj} the number of earthquakes induced by fluid injection estimated as follows: $n_{inj} = n_T - n_{tect} = n_T - S_0\Delta t$, where n_T is the total number of earthquakes during the period Δt and n_{tect} is an estimation of the number of earthquakes in this period generated by tectonic loading. In the same way we estimate the cumulative seismic moment released due to fluid injection $M_{inj} = M_T - M_{tect} = M_T - M_0\Delta t$, where M_T is the total seismic moment released during the period Δt and M_{tect} is an estimation of the cumulative seismic moment released during this phase due to tectonic loading. We should note though that the duration of Phase I is controlled by the injection parameters $\Delta t^I = p_{max}/\beta$, the total diffusion duration depends on p_{max} (see Figure 4b) : $\Delta t^{I+II} \propto p_{max}$ and the duration of Phase II Δt^{II} is the difference between the two: $\Delta t^{II} = \Delta t^{I+II} - \Delta t^I$ (the subscripts refer to the different phases).

During Phase I (Figure 8a1), we observe at first that for a constant injection pressure p_{max}, the number of induced earthquakes and the induced seismic moment released decrease when β increases, as long as β does not exceed the threshold β^*. In this case, the duration of the Phase I decreases as β increases for the same p_{max}, which could explain the observed decrease in n_{inj} and M_{inj}. Beyond β^*, for the same injection pressure p_{max}, as β increases n_{inj} continues to decrease while M_{inj} remains constant. This suggests that the same

seismic moment is released through less numerous events as β increases, which would imply that it is liberated through larger earthquakes. Since β represents the instantaneous variation of the imposed perturbation during Phase I, we would expect it to affect the frequency of the earthquakes and the average moment rate. That is why we estimate the average seismicity rate $\dot{n}^I_{\text{inj}} = (n^I_{\text{inj}})/\Delta t^I$ and the average rate of seismic moment released $\dot{M}^I_{\text{inj}} = (M^I_{\text{inj}})/\Delta t^I$. From Figure 8a2, we observe that in this phase, both the seismicity rate and the moment rate increase at first as β increases. Then, the seismicity rate tends to saturate after the critical threshold β^* (represented by the different stars in this subplot) while the moment rate continues to increase. In this case, larger β can lead to a larger moment rate under a constant seismicity rate increase, suggesting the liberation of the seismic moment through more numerous larger earthquakes, which is coherent with the observations made from Figures 6a–6c where a larger β can increase the frequency of large magnitudes. Moreover, we observe a general systematic increase of n_{inj} and M_{inj} when p_{max} increases as well, especially when $\beta > 1$ MPa/day (Figure 8a1).

During Phase II (Figure 8b), and for small pressure perturbations, we do not observe any clear and significant effect of β on the number of induced earthquakes and the seismic moment released. In this case, n_{inj} and M_{inj} basically depend on the magnitude of the pressure perturbation p_{max}. They both increase with increasing injection pressure when $p_{\text{max}} < 12$ MPa. Beyond it, the number of induced earthquakes increases faster than the increase of M_{inj}, which could explain why the deficit of large magnitudes observed in Figures 6g–6i is more important for large p_{max}. However, for large p_{max}, we observe a dependency on β when it is small ($\beta < 0.1$ MPa/day): n_{inj} and M_{inj} are relatively small, because in this case Phase I was very long in time and Phase II is very short (during Phase I the fluid had enough time to diffuse towards the boundaries so that the time remaining to reach permanent state, that is, Phase II, is very short).

Figure 8c combines the two phases so we can assess the general effect of fluid injection on the induced seismicity. We can thus see that for small injection pressure, the induced seismicity is mainly governed by the injection pressure p_{max}, while for intermediate to large pressure perturbations it is governed by both β and p_{max}: in general a larger p_{max} would induce more numerous events and a higher seismic moment released, a larger β would slightly decrease the number of earthquakes while increasing the seismic moment released, which would lead to the increase in proportion of large magnitudes.

3.3.6. Change in Diffusive Boundary Conditions

As mentioned before, for the results presented so far, we used Dirichlet boundary conditions for the diffusion equation (equation (7)), where we assume that the pore pressure is 0 at the edges of the fault model. We also tested different boundary conditions (Neuman boundary conditions, where we assume that the space derivative of the pore pressure at the fault edge is constant: $\partial p(x, t)/\partial x = k$, in this study $k \approx 10^{-3}$ MPa/m); that is, the flow at the edges is constant. We tested the new boundary conditions for two values of injection pressure ($p_{\text{max}} = 10$ and 14 MPa), with the 14 different values of β. The changes in boundary conditions will modify the pressure profile at the boundaries of the model, but will induce minor modifications for the pressure profile near the injection point during Phases I and II. Furthermore, we will not observe any changes on the pore pressure profile along strike of the fault until later times (after the pressure reaches the edges of the system). Figure S4 in the supporting information represents the comparison for one injection scenario between Dirichlet and Neuman boundary conditions. This change in boundary conditions did not yield any significant change on the seismicity rate which could be related to the observation of Figure 3d that the seismicity rate is mainly perturbed near the injection point. Nonetheless, the change in boundary conditions did not yield any significant changes to the dependence of the magnitude frequency distribution in Phases I and II. During Phase III however, the deficit in large M_w is more pronounced for Neuman boundary conditions, because the mean effective stress $< \sigma_{\text{eff}} >$ in this case is smaller than the one for Dirichlet boundary conditions.

4. Discussion

We presented a coupled numerical model of a heterogeneous planar fault that generates a complex pattern of ruptures of multiple sizes, with a fluid injection-diffusion model. Our model highlights the outcome of fluid flow on the seismicity of the injected fault.

Our results show that the seismicity is immediately disturbed on the onset of fluid injection. This is because in our numerical formulation, the pressure perturbation is directly imposed in the fault. In real cases, a delay would be expected, in order for the pressure perturbation to reach the fault, this delay is generally controlled

by the distance separating the injection well from the preexisting faults, as well as by the permeability of the medium surrounding the fault. Since this is not the case in our numerical formulation, the seismicity rate directly exhibits an enormous increase with time correlated with the increase of pore pressure rate. The seismicity rate reaches a peak (Figure 3e), that generally coincides with the time of the maximum pore pressure rate perturbation (Figure 4a). After this time, even though the pore pressure continues to increase along the fault, the seismicity rate immediately drops because the pressure rate starts to decrease. This is similar to the observed evolution of the seismicity rate in Oklahoma, where the seismicity rate was delayed of several months with respect to changes in injection rate, but correlates with the evolution of the pore pressure rate at 3 km below injection, where the seismicity is detected (Langenbruch et al., 2018). The duration of perturbation is mainly controlled by the fluid diffusion process (Figure 4b). As long as the fluid diffuses along the fault, the pore pressure rate evolves and is not at steady state, the perturbation of seismicity carries on.

Our results also suggest that the induced seismicity is controlled by the injection scenario, similar to the results of Aochi et al. (2014). In our study, the seismicity rate increase appears to depend on the injection parameters p_{max} and β. We found that a larger β can lead to a larger increase of the seismicity rate. For larger β, the pressure rate along the fault is larger and it may drive the fault faster towards failure because it may decrease faster the effective stress along the fault, and hence the frictional strength. However, we observed that β does not seem to have an effect on the seismicity rate increase after a certain threshold β^*. In this case, the increase in stressing rate may be accomodated by changes in the magnitude distribution, with the rate of events staying constant. Hence, for a fixed pressure p_{max}, large values of β can not produce more numerous events (see Figure 5a), however it may produce more frequent large ones. This was observed in Figures 6a–6c and Figures 8a1 and 8a2, where we see that when β increases beyond β^*, the seismicity rate stabilizes while the moment rate continues to increase, which would imply the liberation of seismic moment through larger magnitudes. In an attempt to understand the onset of dynamic slip due to fluid injection, Garagash and Germanovish (2012) studied the direct effect of fluid diffusion on the onset of dynamic slip, while Azad et al. (2017) modeled the onset of dynamic slip due to fault opening in hydraulic fracturing, where no fluid diffusion is taken into account. Garagash and Germanovish (2012) found also that the injection scenario can affect the transition to dynamic slip. They tested different values of constant injection flow rate, and found that higher values can lead to a decrease in the critical time to dynamic slip, hence a higher risk of dynamic rupture for a higher injection rate. Eventhough, in our work we do not look closely at the onset of dynamic rupture, however both our results emphasize on the effect of the injection rate and show how a rapid pressurization increases the probability of larger rupture.

On the other hand, the pore pressure profile along strike depends on the value of p_{max}. For the boundary conditions considered, the mean pressure along the fault can reach $p_{max}/2$. Hence, by increasing the maximum injection pressure p_{max}, we get a larger pore pressure profile along the fault, and ergo a larger decrease of the effective stress and hence the frictional strength according to Equation (2). In this case, the stress drop would be lower, and at constant stressing rate $\dot{\tau}$, it will lead to a higher seismicity rate, thus we would expect the fault to reach instability more frequently. This is observed in our results via the dependency of the seismicity rate increase S_{max}/S_0 on p_{max} observed in Figure 5a, or similarly the dependency of the number of induced earthquakes on p_{max} observed in Figures 8a1, 8b, and 8c. A similar dependency was found by Raleigh et al. (1976) during an in-situ fluid injection experiment in the Rangely Oil field Colorado in 1969, where they tested the effect of the bottom hole pressure and found that by increasing/decreasing it, the resulting frequency of earthquakes increases/decreases as well, respectively. In their experiment the initial reservoir pressure was around 17 MPa, injection started with a bottom hole injection pressure of 27.5 MPa and resulted in an average of 28 earthquakes per month, the injection bottom hole pressure was then decreased to 20 MPa leading to a drop in the seismic activity to one earthquake per month. Later on, they re-increased the pressure to 27.5 MPa and recorded an average of 6 earthquakes per month during this increase, then they maintained it at 28 MPa that lead to an average of 26 earthquakes per month. Although in this case, the pore pressure would not necessarily have reached a steady state, but if we assume that it is the case then the increase in seismicity rate would be in this case $S/S_0 \approx 26/1 \approx 26$, for a pressure perturbation $\Delta p \approx 8$ MPa and $S/S_0 \approx 28/1 \approx 28$ for a pressure perturbation $\Delta p \approx 10$ MPa. This estimate is coherent to what we observe for the seismicity rate increase S_{max}/S_0 when p_{max} is between 8 and 10 MPa if we assume an injection pressure rate $\beta > \beta^*$ (in Figure 5a). This comparison is however very basic and remains limited, since we do not have all the details about the injection procedure and the pressure history at the injection point.

We used the seismicity rate model proposed by Dietrich (1994) to develop an analytical approximation to our case study, which is presented in Appendix C. The basic assumptions of this analytical model is that there is no interactions between the asperities along the fault, and that it does not allow for variations in earthquake magnitude. This analytical model presents the same general trend for the seismicity rate increase as our numerical results, where it shows that the seismicity rate increase depends on both the injection pressure p_{max} and pressure rate β. However, since in this model no interactions are allowed between the different asperities, under pressure perturbation each asperity ruptures independently of the others. This will generate events with the same magnitude and will not allow for very small magnitudes as our model does and no cascade of events is allowed. This may be the cause why this model underestimates the seismicity rate increase with respect to our numerical results. On the other hand, since this formulation does not allow for variations in earthquake magnitude as our model does, the seismicity rate does not saturate for $\beta > \beta^*$, but rather keeps on increasing with β. We should note though that in our formulation of this analytical solution, we did not consider the full equation of the seismicity rate proposed by Dietrich (1994), but rather an approximation (details on the assumption and procedure in Appendix C). In conclusion, since the analytical model does not allow for variations in earthquake magnitude, its application remains restricted and the comparison between the two approaches is limited.

Fluid injection does not only influence the seismicity rate, but it can modify the magnitude frequency distribution of the events as well. The results presented in Figures 3a, 3f, 6, and 7 suggest that both β and p_{max} can influence the magnitude distribution. It shows an increase in the frequency of intermediate and large magnitudes during the first phase, which is directly related to β that acts in this phase. This increase is more and more pronounced for larger β as observed in Figures 6a–6c. This effect of β can be more clearly observed in Figure 7a, where we estimate a lower b value for increasing β. During the second phase however, we observe the effect of p_{max} on the magnitude distribution, where we see that a higher p_{max} can lead to less frequent large events. A systematic increase of the b value was observed with increasing p_{max} in this phase, that is, with decreasing the effective normal stress, and thus decreasing differential stress. A similar relation was observed between the b value and the increasing differential stress with depth, for laboratory experiments (Scholz, 1968), as well as for earthquake statistics for different continental regions (Gerstenberger et al., 2001; Spada et al., 2013). Scholz (2015) proposed the following inverse relation between the b value and the differential stress that can explain the b-depth variability for California, Switzerland, Italy, Greece, Turkey and Japan: $b = 1.23 \pm 0.06 - (0.0012 \pm 0.0003)(\sigma_1 - \sigma_3)$. If we assume an average variation of the b value, we get $b_{numerical} \approx 0.76 - 0.005(\sigma_1 - \sigma_3)$ ($\sigma_1 - \sigma_3 \approx \mu_0 \sigma_{eff} = 0.6 \sigma_{eff}$). The b values obtained here are larger by a factor of around 2 than the one estimated by Scholz (2015). This discrepancy could be due to multiple causes: (1) in our numerical formulation, we model VW patches, the size of which follow a power law distribution with a -2 exponent. This distribution could influence the rupture sizes and thus the b value; (2) in a 2-D formulation, the redistribution of stress following a rupture are generally overestimated with respect to 3-D formulation, which tends to increase the b value. What controls the absolute value of b is not the purpose of this study, and requires more attention. Here we insist on the relative b value changes, which are of the same magnitude ($\approx 10^{-3}(\sigma_1 - \sigma_3)$).

Postinjection seismicity remains nowadays an open subject, for instance the seismicity in Basel (Deichman & Giardini, 2009) or the seismicity in Youngstown, Ohio (Kim, 2013). In our numerical model, the injection shut in leads to a decrease of the number of earthquakes with respect to the one before injection began, where the pore pressure diffused out of the fault. However, our numerical model is confined in the vicinity of the fault, and we do not explore what happens in the surrounding region. Thus, our model is not capable to predict the seismic activity after shut in, for surrounding fractures or faults, and therefore unable to explain postinjection seismicity as was discussed by Baisch et al. (2010), McClure and Horne (2011) and Dietrich et al. (2015). For that reason, we did not analyze in details the characteristics of seismicity after shut-in.

Furthermore, it was observed that aseismic slip can in some cases drive postinjection activity (Bourouis & Bernard, 2007). Eventhough, we observed in our results some slow aseismic slip episodes (Figures 3c and 3d), the role of aseismic slip in injection induced seismicity and the way it is perturbed by fluid injection were not the purpose of this study. This demands more work and it remains to be investigated in future studies.

Additionally, in our modeling approach, we assumed a constant value of the diffusivity $D = 0.005$ m^2/s. A lower value of diffusivity would induce lower pore pressure rates along the fault, and since in our model the time series of the seismicity rate is correlated to the pore pressure rate, then we would expect to have a lower

seismicity rate in this case. We conducted some tests on the same fault model with another diffusivity value $D_2 = 0.1D$ and found that in this case for the same p_{max}, S_{max}/S_0 saturates at lower values. However, a lower diffusivity will lead to a larger diffusion time, and hence a larger Phase II in time. We are not sure how this increase in duration until steady state will affect the number of induced earthquakes and the cumulative seismic moment released. This issue deserves more analysis and we leave it for further studies. Moreover, in our modeling approach the considered diffusivity does not evolve in time. However, the permeability, and consequently the diffusivity, along the fault, can change following a seismic event and slip accumulation (Baghbanan & Jing, 2008; Zhang & Tullis, 1998), or reduction in vertical effective stress due to fluid injection (Fisher & Zwart, 1996; Ghabezloo et al., 2009; Rutter & Mecklenburgh, 2018; Zoback & Byerlee, 1975). Thus, our model does not allow modeling of shear induced fluid flow for instance, or permeability enhancement. Future works and development of our numerical model would be to include a slip and stress dependent diffusivity.

Finally, we should note that we only tested one fault parametrization. It would be interesting for future work to test different fault configurations and to study how this would affect the resulting induced seismicity.

5. Conclusion

We proposed a continuous rate- and state-dependent 2-D model of a heterogeneous fault, that can generate a complex pattern of ruptures with different sizes, coupled with an injection-diffusion model. Our model emphasizes on the consequences of the fluid injection history on seismicity and highlights some key parameters. In particular, we showed that the fluid injection disrupts the state of the fault. It leads to a sharp increase in the seismicity, as well as an increase in the proportion of large magnitudes. Our results suggest that the seismicity rate follows the variation of the pore pressure rate, which was observed recently for the seismicity rate in Oklahoma. The seismicity perturbation stops when the pressure reaches a steady state along the fault. We also pointed out that magnitude frequency distribution of events is sensitive to the evolution of the pore pressure and pore pressure rate along the fault. The injection scenario has a significant effect on the seismicity rate and the magnitudes of the events as well. Larger injection pressure p_{max} leads to a larger amplification of the seismicity rate, and hence to more numerous events, however it may cause a deficit in the frequency of large magnitudes M_w. On the other hand, the seismicity rate increases with increasing the injection pressure rate β, until a certain threshold β^*. Beyond it, the amplification of the seismicity rate saturates, while the seismic moment is released through larger earthquakes. This suggests that there is a tradeoff between the number of the induced earthquakes and the magnitudes of the events at the scale of a single fault. Finally, we conducted a comparison between our model and the seismicity rate model proposed by Dietrich (1994) and showed that the latter predicts a close dependency of the induced seismicity rate on the injection parameters, however it is not able to model the tradeoff between the magnitudes and the number of the induced earthquakes since it does not allow for variation in the magnitude content.
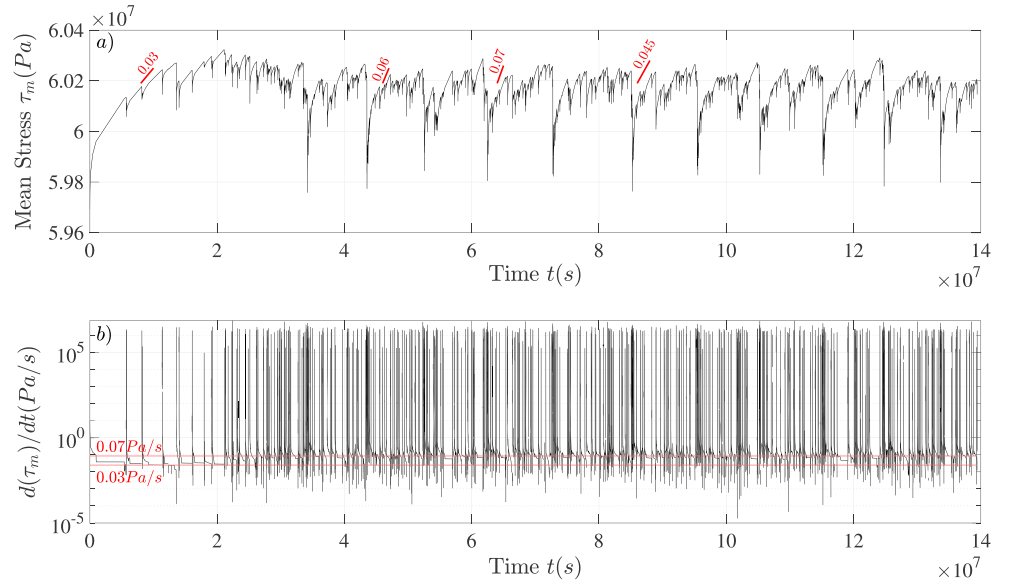
Appendix A: Analytical Solution of the Diffusion Equation

In the following, we give the solution of the diffusion equation (equation (7)) for half the fault model presented in Figure 1a, where $x = 0$ and $x = L = L_0/2$ represent the injection point (center of the fault), and the right edge of the fault, respectively. We solve the two phases ($t_i < t < t_r$) and ($t > t_r$), separately, using Dirichlet boundary conditions: $p(L, t) = 0$.

A1. Injection Phase 1 ($t_i < t < t_r$):

Let $p_1(x, t)$ be the solution of the diffusion equation in Phase 1. In this phase, the boundary conditions are: $p_1(0, t) = \beta t, p_1(L, t) = 0$, while the initial conditions are $p_1(x, 0) = 0$. The boundary conditions are nonhomogeneous and time-dependent. We assume that the solution is a summation of a steady state solution $w_1(x, t)$ and a transient state solution $v_1(x, t)$, which is a time-dependent summation of sine functions, as follows:

$$p_1(x, t) = w_1(x, t) + v_1(x, t) = \beta t \left(1 - \frac{x}{L}\right) + \frac{2\beta L^2}{\pi^3 D} \sum_{n=1}^{+\infty} \left(\frac{\left(e^{-D\left(\frac{n\pi}{L}\right)^2 t} - 1\right)}{n^3}\right) \sin\left(\frac{n\pi x}{L}\right). \quad (A1)$$

Figure B1. (a) Time series of the mean stress τ_m along the fault. (b) Time derivative of the mean stress $\mathrm{d}(\tau_m)/\mathrm{d}t$ (only the positive gradient is plotted).

A2. Injection Phase 2 ($t_r < t$):

Let $p_2(x, t)$ be the solution of the diffusion equation in Phase 2. In this phase, the boundary conditions are: $p_2(0, t) = p_{\max}$, $p_2(L, t) = 0$, while the initial conditions are $p_2(x, 0) = p_1(x, t_r)$. Similarly, we assume that the solution is a summation of a steady state solution $w_2(x, t)$ and a transient state solution $v_2(x, t)$, which is a time-dependent summation of sine functions, as follows:

$$p_2(x, t) = w_2(x, t) + v_2(x, t) = p_{\max}\left(1 - \frac{x}{L}\right) + \frac{2\beta L^2}{\pi^3 D} \sum_{n=1}^{+\infty}\left(\left(\frac{e^{-D\left(\frac{n\pi}{L}\right)^2 t_r} - 1}{n^3}\right) e^{-D\left(\frac{n\pi}{L}\right)^2 t} \sin\left(\frac{n\pi x}{L}\right)\right). \qquad \text{(A2)}$$

Appendix B: Estimation of the Background Stressing Rate

In order to estimate the background stressing rate $\dot\tau_0$ acting on our fault model, we look closely to the evolution of the mean stress τ_m along the fault, along with its time derivative $\mathrm{d}(\tau_m)/\mathrm{d}t$. We estimate τ_m at each time step using the rate- and state- formulation from equation (2). The time series of τ_m and $\mathrm{d}(\tau_m)/\mathrm{d}t$ are represented in Figures B1a and B1b over a period of 4.5 years, without fluid injection. We can observe that during the interseismic period, the mean stress τ_m increases quasi-linearly following a constant $\mathrm{d}(\tau_m)/\mathrm{d}t$. However, $\mathrm{d}(\tau_m)/\mathrm{d}t$ varies in the range [0.03–0.07] Pa/s.

Appendix C: Analytical Seismicity Rate model following (Dietrich, 1994)

Dietrich (1994) proposed an analytical model for the seismicity rate following stress perturbations, with rate- and state-dependent fault properties. The basic assumptions of this analytical model are that the seismicity originates for a population of identical asperities modelled as rate and state spring slider systems, the faults are close to failure and do no interact (no stress transfer). Thus, it does not allow for variations in earthquake magnitude. In his formulation, the seismicity rate R_D obeys

$$R_D = \frac{r}{\gamma\dot\tau}, \qquad \text{(C1)}$$

where r is the steady state seismicity rate under constant reference stressing rate $\dot\tau$ acting on the faults and γ is a state variable that depends on both time and stressing history, following

$$\mathrm{d}\gamma = \frac{1}{a(\sigma - p)}\left(\mathrm{d}t - \gamma\mathrm{d}\tau + \gamma\left(\frac{\tau}{\sigma - p} - \alpha\right)\mathrm{d}(\sigma - p)\right), \qquad \text{(C2)}$$

where a is the rate and state constitutive parameter, σ is the normal stress, p is the pore pressure, τ is the shear stress and α is a nondimensional constant (Linker & Dietrich, 1992). From equation (2), we have $\tau/(\sigma - p) = \mu$, and in the following we assume that $\mu \approx \mu_0$ (given the small values of a and b considered). We also assume that $p \ll \sigma$ and thus $\sigma - p \approx \sigma$, since for the largest injection pressure $p_{max} = 20$ MPa, the mean pressure along the fault is 10 MPa, and $p - \sigma = 0.9\sigma$. Dividing equation (C2) by dt, we get

$$\dot{\gamma} = \frac{1}{a\sigma} - \frac{\gamma}{a\sigma}\left(\left(\mu_0 - \alpha\right)\dot{p} + \dot{\tau}\right). \tag{C3}$$

In this study we estimate the seismicity rate from this model using the values of constant background stressing rate $\dot{\tau} = 0.03$ and 0.07 Pa/s (see Appendix B for details). This equation presents two different solutions during injection Phase I and II.

C1. Injection Phase 1 ($t_i < t < t_r$)

$$\gamma_1(x, t) = \frac{1}{\tau_r}e^{-\lambda_1(x,t)} + \frac{1}{a\sigma}e^{-\lambda_1(x,t)}\int_0^t e^{\lambda_1(x,t')}dt' \tag{C4}$$

where $\lambda_1(x, t) = \frac{\mu_0 - \alpha}{a\sigma}p_1(x, t) + \frac{\dot{\tau}t}{a\sigma}$, and $p_1(x, t)$ is the solution of the pressure diffusion in the Phase I from equation (A1).

C2. Injection Phase 2 ($t_r < t$)

$$\gamma_2(x, t) = \gamma_1(x, t_r)e^{\lambda_1(x,t_r)-\lambda_2(x,t)} + \frac{1}{a\sigma}e^{-\lambda_2(x,t)}\int_{t_r}^t e^{\lambda_2(x,t')}dt' \tag{C5}$$

where $\lambda_2(x, t) = \frac{\mu_0 - \alpha}{a\sigma}p_2(x, t) + \frac{\dot{\tau}t}{a\sigma}$, and $p_2(x, t)$ is the solution of the pressure diffusion in the Phase II from equation (A2).

In order to apply this model, we should choose the number of asperities n (i.e., number of spring slider systems) used. In this case, the background seismicity rate is $S_i = S_0/n$ on each asperity. Then we estimate the time series of the state variable at the center of the asperity i: $\gamma_i(t)$. Then similarly we estimate the seismicity rate $R_{D_i}(t)$ from equation (C1). Finally, we sum the different seismicity rate $R_{D_i}(t)$ on all the asperities in order to have the general seismicity rate governing the fault $R_D = \Sigma_{i=1}^n R_{D_i}(t)$.

References

Abercrombie, R., & Rice, J. (2005). Can observations of earthquake scaling constrain slip weakening? *Geophysical Journal International*, *162*, 406–424.

Aki, K. (1965). Maximum likelihood estimate of b in the formula $\log n = a - bm$ and its confidence limits. *Bulletin of the Earthquake Research Institute*, *43*, 237–239.

Aochi, H., Poisson, B., Toussaint, R., Rachez, X., & Schmittbuhl, J. (2014). Self-induced seismicity due to fluid circulation along faults. *Geophysical Journal International*, *196*, 1544–1563.

Azad, M., Garagash, D., & Satish, M. (2017). Nucleation of dynamic slip on a hydraulically fractured fault. *Journal of Geophysical Research: Solid Earth*, *122*, 2812–2830. https://doi.org/10.1002/2016JB013835

Bachmann, C., Wiemer, S., Woessner, J., & Hainzl, S. (2011). Statistical analysis of the induced Basel 2006 earthquake sequence: Introducing a probability-based monitoring approach for enhanced geothermal systems. *Geophysical Journal International*, *186*, 793–807.

Baghbanan, A., & Jing, L. (2008). Stress effects on permeability in a fractured rock mass with correlated fracture length and aperture. *International Journal of Rock Mechanics & Mining Sciences*, *45*, 1320–1334.

Baisch, S., Voros, R., Rothert, E., Stang, H., Jung, R., & Schellschmidt, R. (2010). A numerical model for fluid injection induced seismicity at Soultz-Sous-Forets. *International Journal of Rock Mechanics & Mining Sciences*, *47*, 405–413.

Barbour, A., Norbeck, J., & Rubinstein, J. (2017). The effects of varying injection rates in Osage County, Oklahoma, on the 2016 M_w 5.8 Pawnee earthquake. *Seismological Research Letters*, *88*(4), 1040–1053.

Bourouis, S., & Bernard, P. (2007). Evidence for coupled seismic and aseismic fault slip during water injection in the geothermal site of Soultz (France), and implications for seismogenic transients. *Geophysical Journal International*, *169*, 723–732.

Byerlee, J. (1978). Friction of rocks. *Pure and Applied Geophysics*, *116*, 615–626.

Chang, K., Yoon, H., & Martinez, M. J. (2018). Seismicity rate surge on faults after shut-in: Poroelastic response to fluid injection. *Bulletin of the Seismological Society of America*, *108*(4), 1889–1904.

Cochard, A., & Rice, J. (1997). A spectral method for numerical elastodynamic fracture analysis without spatial replication of the rupture event. *Journal of the Mechanics and Physics of Solids*, *45*(8), 1393–1418.

Davis, S., & Frohlich, C. (1993). Did (or will) fluid injection cause earthquakes? Criteria for a rational assessment. *Seismological Research Letters*, *64*(3-4).

Deichman, N., & Giardini, D. (2009). Earthquakes induced by the stimulation of an enhanced geothermal system below Basel (Switzerland). *Seismological Research Letters*, *80*(5), 784–798.

Dempsey, D., & Riffault, J. (2019). Response of induced seismicity to injection rate reduction: Models of delay, decay, quiescence, recovery, and Oklahoma. *Water Resources Reserach*, *55*, 656–681. https://doi.org/10.1029/2018WR023587

Dietrich, J. (1979). Modeling of rock friction. 1. Experimental results and constitutive equations. *Journal of Geophysical Research*, *84*(B5), 2161–2168.

Dietrich, J. (1994). A constitutive law for rate of earthquake production and its application to earthquake clustering. *Journal of Geophysical Research*, *99*(B2), 2601–2618. https://doi.org/10.1029/93JB02581

Dietrich, J., Richards-Dinger, K., & Kroll, K. (2015). Modeling injection-induced seismicity with the physics-based earthquake simulator RSQSim. *Seismological Research Letters*, *86*(4), 1102–1109.

Dublanchet, P. (2018). The dynamics of earthquake precursors controlled by effective friction. *Geophysical Journal International*, *212*(2), 853–871.

Ellsworth, W. (2013). Injection-induced earthquakes. *Science*, *341*(6142), 1225942.

Fehlberg, E. (1969). Low-order classical Runge-Kutta formulas with step size control and their application to some heat transfer problems (Nasa Technical Report). United States.

Fisher, A., & Zwart, G. (1996). Relation between permeability and effective stress along a plate-boundary fault, Barbados accretionary complex. *Geology*, *24*(4), 307–310.

Frohlich, C. (2012). Two-year survey comparing earthquake activity and injection-well locations in the Barnett Shale, Texas. *Proceedings of the National Academy of Sciences of the United States of America*, *109*, 13,934–13,938.

Frohlich, C., Ellsworth, W., Brown, W., Brunt, M., Luetgert, J., MacDonald, T., & Walter, S. (2014). The 17 May 2012 M4.8 earthquake near Timpson, East Texas: An event possibly triggered by fluid injection. *Journal of Geophysical Research: Solid Earth*, *119*, 581–593. https://doi.org/10.1002/2013JB010755

Garagash, D., & Germanovish, L. (2012). Nucleation and arrest of dynamic slip on a pressurized fault. *Journal of Geophysical Research*, *117*, B10310. https://doi.org/10.1029/2012JB009209

Gerstenberger, M., Wiemer, S., & Giardini, D. (2001). A systematic test of the hypothesis that the *b* value varies with depth in California. *Geophysical Research Letters*, *28*(1), 57–60.

Ghabezloo, S., Sulem, J., Guedon, S., & Martineau, F. (2009). Effective stress law for the permeability of a limestone. *International Journal of Rock Mechanics and Mining Sciences*, *46*, 297–306.

Hanks, T., & Kanamori, H. (1979). A moment magnitude scale. *Journal of Geophysical Research*, *84*(B5), 2348–2350.

Healy, J., Rubey, W., Griggs, D., & Raleigh, C. (1968). Disposal of waste fluids by injection into a deep well has triggered earthquakes near Denver, Colorado. *Science*, *161*(3848), 1301–1310.

Hermann, R., Park, S.-K., & Wang, C.-Y. (1981). The Denver earthquakes of 1967–1968. *Bulletin of the Seismological Society of America*, *71*(3), 731–745.

Holland, A. (2011). Examination of possibly induced seismicity from hydraulic fracturing in the Eola Field, Garvin County, Oklahoma. Oklahoma Geological Survey open-file report of1-2011 ed.

Horton, S. (2012). Disposal of hydrofracking waste fluid by injection into subsurface aquifers triggers earthquake swarm in central Arkansas with potential for damaging earthquake. *Seismological Research Letters*, *83*(2), 250–260.

Hubert, M., & Rubey, W. (1959). Mechanics of fluid-filled porous solids and its application to overthrust faulting. *Bulletin of the Geological Society of America*, *70*, 115–166.

Ide, S., & Aochi, H. (2005). Earthquakes as multiscale dynamic ruptures with heterogeneous fracture surface energy. *Journal of Geophysical Research*, *110*, B11303. https://doi.org/10.1029/2004JB003591

Ikari, M., Saffer, D., & Marone, C. (2009). Frictional and hydrologic properties of a major splay fault system, Nankai subduction zone. *Geophysical Research Letters*, *36*, L20313. https://doi.org/10.1029/2009GL040009

Jaeger, J., Cook, N., & Zimmerman, R. (2007). *Fundamentals of rock mechanics*. Oxford: Blackwell Publishing.

Kanamori, H., & Hauksson, E. (1992). A slow earthquake in the Santa Maria basin, California. *Bulletin of the Seismological Society of America*, *85*(2), 2087–2096.

Keranen, K., Savage, H., Abeys, G., & Cochran, E. (2013). Potentially induced earthquakes in Oklahoma, USA: Links between wastewater injection and the 2011 M_W 5.7 earthquake sequence. *Geology*, *41*(6), 699–702.

Kim, W.-Y. (2013). Induced seismicity associated with fluid injection into a deep well in Youngstown, Ohio. *Journal of Geophysical Research: Solid Earth*, *118*, 3506–3518. https://doi.org/10.1002/jgrb.50247

Kroll, K., Richards-Dinger, K., & Dietrich, J. (2017). Sensitivity of induced seismic sequences to rate-and-state frictional processes. *Journal of Geophysical Research: Solid Earth*, *122*, 207–219. https://doi.org/10.1002/2017JB014841

Langenbruch, C., Weingarten, M., & Zoback, M. (2018). Physics-based forecasting of man-made earthquake hazards in Oklahoma and Kansas. *Nature Communications*, *9*, 3946.

Langenbruch, C., & Zoback, M. (2016). How will induced seismicity in Oklahoma respond to decreased saltwater injection rates? *Science Advances*, *2*, e1601542.

Linker, M., & Dietrich, J. (1992). Effects of variable normal stress on rock friction: Observations and constitutive equations. *Journal of Geophysical Research*, *97*(B4), 4923–4940.

Majer, E., Baria, R., Stark, M., Oates, S., Bommer, J., Smith, B., & Asanuma, H. (2007). Induced seismicity associated with enhanced geothermal systems. *Geothermics*, *36*, 185–222.

Marone, C. (1998). Laboratory-derived friction laws and their application to seismic faulting. *Annual Review of Earth and Planetary Sciences*, *26*, 643–96.

McClure, M., & Horne, R. (2011). Investigation of injection-induced seismicity using a coupled fluid flow and rate/state friction model. *Geophysics*, *76*(6), WC181–WC198.

McGarr, A. (2014). Maximum magnitude earthquakes induced by fluid injection. *Journal of Geophysical Research: Solid Earth*, *119*, 1008–1019. https://doi.org/10.1002/2013JB010597

Ohnaka, M. (2003). A constitutive scaling law and a unified comprehension for frictional slip failure, shear fracture of intact rock, and earthquake rupture. *Journal of Geophysical Research*, *108*(B2), 2080. https://doi.org/10.1029/2000JB000123

Raleigh, C., Healy, J., & Bredehoeft, J. (1976). An experiment in earthquake control at Rangely, Colorado. *Science*, *191*, 1230–1237.

Rice, J. (1993). Spatio-temporal complexity of slip on a fault. *Journal of Geophysical Research*, *98*(B6), 9885–9907.

Rice, J., & Ruina, A. (1983). Stability of steady frictional slipping. *Journal of Applied Mechanics*, *50*, 343–349.

Rubin, A., & Ampuero, J.-P. (2005). Earthquake nucleation on (aging) rate and state faults. *Journal of Geophysical Research*, *110*, B11312. https://doi.org/10.1029/2005JB003686

Rubinstein, J., Ellsworth, W., & McGarr, A. (2012). The 2001–present triggered seismicity sequence in the Raton Basin of southern Colorado/northern New Mexico. *Bulletin of the Seismological Society of America*, *104*, 2162–2181.

Ruina, A. (1983). Slip instability and state variable friction laws. *Journal of Geophysical Research*, *88*(B12), 10,359–10,370.

Rutqvist, J., Rinaldi, A., Cappa, F., & Moridis, G. (2013). Modeling of fault reactivation and induced seismicity during hydraulic fracturing of shale-gas reservoirs. *Journal of Petroleum Science and Engineering*, *107*, 31–44.

Rutter, E., & Mecklenburgh, J. (2018). Influence of normal and shear stress on the hydraulic transmissivity of thin cracks in a tight quartz sandstone, a granite, and a shale. *Journal of Geophysical Research: Solid Earth*, *123*, 1262–1285. https://doi.org/10.1002/2017JB014858

Scholz, C. (1968). The frequency-magnitude relation of microfracturing in rock and its relation to earthquakes. *Bulletin of the Seismological Society of America*, *58*(1), 399–415.

Scholz, C. (2015). On the stress dependence of the earthquake *b* value. *Geophysical Research Letters*, *42*, 1399–1402. https://doi.org/10.1002/2014GL062863

Segall, P., & Lu, S. (2015). Injection-induced seismicity: Poroelastic and earthquake nucleation effects. *Journal of Geophysical Research: Solid Earth*, *120*, 5082–5103. https://doi.org/10.1002/2015JB012060

Shi, Y., & Bolt, B. (1982). The standard error of the magnitude-frequency *b* value. *Bulletin of the Seismological Society of America*, *72*(5), 1677–1687.

Simpson, D. (1986). Triggered earthquakes. *Annual Review of Earth and Planetary Sciences*, *14*, 21–42.

Skoumal, R., Brudzinski, M., Currie, B., & Levy, J. (2014). Optimizing multi-station earthquake template matching through re-examination of the Youngstown, Ohio, sequence. *Earth and Planetary Science Letters*, *405*, 274–280.

Spada, M., Tormann, T., Wiemer, S., & Enescu, B. (2013). Generic dependence of the frequency-size distribution of earthquakes on depth and its relation to the strength profile of the crust. *Geophysical Research Letters*, *40*, 709–714. https://doi.org/10.1029/2012GL054198

Sumy, D., Cochran, E., Keranen, K., Wei, M., & Abers, G. (2014). Observations of static Coulomb stress triggering of the November 2011 *M*5.7 Oklahoma earthquake sequence. *Journal of Geophysical Research: Solid Earth*, *119*, 1904–1923. https://doi.org/10.1002/2013JB010612

Turcotte, D., & Schubert, G. (2014). *Geodynamics*. Cambridge: Cambridge University Press.

Turuntaev, S., & Riga, V. (2017). Non-linear effects of pore pressure increase on seismic event generation in multi-degree-of-freedom rate-and-state model of tectonic fault sliding. *Nonlinear Processes in Geophysics*, *24*, 215–225.

Van der Elst, N., Savage, H., Keranen, K., & Abers, G. (2013). Enhanced remote earthquake triggering at fluid-Injection sites in the midwestern United States. *Science*, *341*(6142), 164–167.

Viegas, G., Buckingham, K., Baig, A., & Urbancic, T. (2012). Large scale seismicity related to wastewater injection near Trinidad, Colorado, USA, Calgary, Alberta, Canada.

Yeck, W., Weingarten, M., Benz, H., McNamara, D., Bergman, E., Hermann, R., et al. (2016). Far-field pressurization likely caused one of the largest injection induced earthquakes by reactivating a large preexisting basement fault structure. *Geophysical Research Letters*, *43*, 10,198–10,207. https://doi.org/10.1002/2016GL070861

Zhang, S., & Tullis, T. (1998). The effect of fault slip on permeability and permeability anisotropy in quartz gouge. *Tectonophysics*, *295*, 41–52.

Zoback, M. D., & Byerlee, J. D. (1975). Permeability and effective stress. *AAPG Bulletin*, *59*, 154–158.